Exploring Radarsat-2 SAR Cross-Polarization Ratio Capability for Tundra Snow Depth Estimation Using Numerical and Deep Learning Approach

by

Yuanhao Cao

A thesis
presented to the University of Waterloo
in fulfillment of the
thesis requirement for the degree of
Master of Science
in
Geography

Waterloo, Ontario, Canada, 2023

Author's Declaration

I hereby declare that I am the sole author of this thesis. This is a true copy of the thesis, including any required final revisions, as accepted by my examiners.

I understand that my thesis may be made electronically available to the public.

Abstract

Snow is essential to the Earth's system, significantly influencing the global climate, freshwater availability, and economic activities. A significant snow cover decline has been reported in vast northern hemisphere areas. The decrease in snow cover will affect more than one-sixth of the world's population who rely on the snow as a freshwater supplement. Snow mass, often expressed as snow water equivalent (SWE), signifies the quantity of water held in the form of snow on the Earth's surface, and it plays a crucial role in the functioning of water, energy, and geochemical processes. Since the seasonal snow has a high spatial variability at regional and local scales, surface observations cannot provide sufficient SWE information. The quality of global SWE estimates needs to be improved. In recent years, C-band spaceborne SAR has shown a high potential for global monitoring of SWE. This thesis aims to explore the current spaceborne C-band SAR signal sensitivity to Arctic tundra snow and define a suitable approach for estimating deep snow depth through the tundra environment. The noticeable variation of C-band backscatter with the snow depth generally demonstrated the C-band sensitivity to dry snow for the deep snow. These areas are dominated by tall vegetation areas such as tall shrubs and riparian shrubs. The cross-polarization ratio method also shows a higher correlation with snow depth than cross-pol and co-pol backscatter, which is generally consistent with earlier research. Also, numerical, and deep learning (DL) approaches were tested based against drone-based snow depth reference data. The result shows that the numerical approach may only be valid in a place with over 2.5 m snowpack. Compared to the numerical approach, the DL approach shows a better evaluation, resulting in a correlation coefficient of R 0.79 between the estimated and target snow depth with a root mean square error (RMSE) of 19 cm. The DL approach can be more suitable for estimating snow depth from C-band SAR observation under the Arctic tundra snow environment.

Acknowledgements

First and foremost, I am deeply grateful to my supervisor, Dr. Richard Kelly, whose guidance and mentorship were invaluable throughout this process. Giving me the funding and opportunity to do research and providing instructive guidance throughout my undergraduate and graduate study in University of Waterloo. Without Dr. Kelly's support, this work would not have been possible.

I am also indebted to my committee members, Dr. Jonathan Li, Professor at the Department of Geography and Environmental Management, University of Waterloo, and Dr. Benoit Montpetit, from Environment and Climate Change Canada, Climate Research Division, for their careful review of my work and their insightful feedback in the thesis defense.

My special thanks to Dr. Shurun Tan, assistant professor at Zhejiang University-University of Illinois Urbana-Champaign Institute, Zhejiang University, and Dr. Qinghuan Li, Post-doctoral fellow at Department of Geography and Environmental Management, University of Waterloo, their suggestions, and critiques helped me to improve the quality of this thesis significantly.

I would like to express my sincere appreciation to Branden Walker and Dr. Philip Marsh from Cold Regions Research Centre, Wilfrid Laurier University, Dr. Benoit Montpetit and Dr. Joshua King, from Environment and Climate Change Canada, Climate Research Division, Wei Wang, Ph.D. candidate at Department of Geography and Environmental Management, University of Waterloo, for providing access to the datasets that this project is based on. Their generosity was essential to the success of this research.

I am grateful for the collaboration and support of my fellow group members, Aaron, Jeff, Akash, Lina, Zeinab, Margot and Vicky. Sharing ideas, discussing challenges, and providing motivation made this entire process more enjoyable and enriching.

Finally, I want to express my deepest gratitude to my family members, especially my wife, Jiayi. Their unwavering love, support, and understanding were the foundation upon which I could build this project. I am truly blessed to have them by my side.

This work is a testament to the power of collaboration and support. I am grateful to each and every one of you for your contributions to this project.

Table of Contents

List of Figures

List of Tables

Chapter 1 Introduction

1.1 Research Context and Motivation

Terrestrial snow is a critical component of the Earth's system, which significantly influences the global climate system, freshwater availability, and even economics (Sturm et al., 2017). Seasonal snow covers an average of 46 x 10^6 km^2 of Earth's surface (31% of the land area) each winter. According to the recent IPCC sixth assessment report (2021), climate change is having an increasing impact on global snow cover extent and duration, especially in the Artic, where changes occur at rates nearly twice that of the rest of the world (Derksen & Brown, 2012). Over the past few years, there has been a 13% reduction in spring snow cover per decade. Furthermore, given that over one-sixth of the global population depends on freshwater sourced from snow and glaciers, it is highly probable that the availability of this water resource will decrease in the coming century (Tsang et al., 2022). Quantifying snow cover and mass is essential for understanding climate change, weather services, and water management of the earth system.

Snow plays a vital role in the surface energy budget in the climate system due to the high albedo of snow. When the snow covers the surface, a large amount of solar radiation will be reflected to the atmosphere, helping to regulate the Earth's temperature. As seasonal snow cover melts, the surface reflects much less radiation, leading to more radiation absorption; this positive feedback loop is called snow-albedo feedback (Armstrong & Brun, 2008). Between 1972 and 1992, the mean annual SCE (snow cover extent, also referred to as the area covered by the snow) decreased by about 10% due to the high spring melt rates (Groisman et al., 1994). After that, a continuous decreasing trend of SCE has also been observed. The decrease of SCE mainly occurs in the spring and fall, and the most vital reductions occur in May and June (Mudryk et al., 2017). Until 2019, SCE in May and June decreased at rates of 3.1% and 13.6% per decade respectively (Bormann et al., 2018). As a result of the strong relationship between energy budget and snow, changes in seasonal SCE indicate short-term weather and long-term climate changes at regional and global scales.

In addition to its role in the climate system, snow is an essential freshwater resource. Snow accumulates on mountains, and the snowmelt runoff in spring and summer provides freshwater for many regions, especially the northern hemisphere. In the Himalayas, meltwater plays a crucial role in meeting the freshwater needs of approximately 1.4 billion individuals in countries such as China and India (DeBeer & Pomeroy, 2017). Snow mass changes can significantly impact areas that rely on seasonal snowmelt for water. In hydrology, the amount of water in a given snow volume is called SWE (snow water equivalent also refers to snow mass). SWE and snow depth are convertible within known bulk density (Sturm et al., 2010), the equation is shown as:

$$SWE = snow\ depth * snow\ density \tag{1.1}$$

Hydrological modelling and streamflow forecasting require SWE information and its spatial distribution to quantify the contribution of snowmelt to local water resources. Unlike SCE, SWE has a high spatial variability at regional scale, but the general decrease of SWE has been observed across the Northern Hemisphere (Kunkel et al., 2016). In Europe, station-based snow depth decreased by about 12% per decade from 1951 to 2017 (Fontrodona et al., 2018). In North America, long-term station data exhibit decreasing trends over the last six decades, with an average decline of 15–30% (Mote et al., 2018). In Canada, similar decrease trends in SWE are found across Eastern and Northern Canada, with a 5 to 10% decrease per decade, but the increased SWE is obtained in the western area (Mudryk et al., 2018). Further, the decreases in spring and summer SWE have been observed in high mountain Asia (Smith et al., 2018). Thus, changing SWE has led to changes in the hydrologic cycle, affecting water resource management, and increasing the risk of floods and droughts wherever in a global and local scale.

Due to the importance of SCE and SWE monitoring, obtaining high-precision spatio-temporal variability of snow parameters is significant for climate change research, water resource management in river basins, ecological environment assessment, and snow disaster forecast and evaluation. Currently, the most used measurements of snow parameters are in-situ measurement and remote sensing observation (Awasthi & Varade, 2021). Traditionally, the in-

situ measurement is the primary method to obtain the SCE and SWE information, including meteorological station and field measurements. The station observations could provide continuous monitoring of snow precipitation, snow depth on the ground, snow density and other relative parameters from the daily, monthly, or annual scale, but the station measurements can only provide accurate measurements on a limited spatial coverage (Kinar & Pomeroy, 2015). Field experiments have been used to characterize snow information in places with no station data, providing more detailed information (such as grain size and snow layering) from the snow pit. However, field campaigns are time-consuming and expensive, especially compared to automatic station measurements (Sturm et al., 2010; Odry et al., 2020), and cannot provide wide area spatio-temporal observations. Seasonal snow cover at high latitude high-altitude, and inaccessible areas, is difficult to measure and is often characterized by variable structure and properties and irregular thickness and distribution (Liu et al., 2021). This makes it difficult to obtain large-scale snow depth data accurately and efficiently by using field observations, station observations and model predictions that rely on in situ measurements. Therefore, remote sensing (RS) technology has the advantage of observing snow rapidly, and in multi-temporal and multi-spectral domains. In areas with insufficient meteorological data and harsh climatic conditions, the RS is the most significant method that can reflect the status and changes of large-scale snow cover (Foster, et al., 2011).

Currently, most of the RS measurement bands used in SCE and SWE mainly focus on the optical and microwave (Awasthi & Varade, 2021). Usually, optical remote sensing is used to extract snow extent, and the visible and near-infrared band is highly vulnerable to solar radiation and weather conditions such as clouds and rain. Since visible light and near-infrared radiation signals cannot penetrate snow, and the optical properties of ice and snow are similar, snow reflectivity in these bands is not sensitive to information such as depth and liquid content in the snowpack (except for very shallow snow), which is the biggest weakness of optical remote sensing (Tsang et al. 2022). Since the measurement of SWE is difficult to obtain by optical remote sensing, microwave RS is essential for studying SWE. Unlike visible light and near-infrared sensors, microwave instruments have nearly all-weather observation capabilities,

and microwaves have strong penetrating capabilities, overcoming the impact of visible light and near-infrared remote sensing on the atmosphere and the confusion of clouds on snow (Tsang et al, 2022). Microwaves have a high sensitivity to object scattering, making them superior to visible light and near-infrared bands in obtaining SWE and internal property information of snow layers, which also allows microwave methods to retrieve snow-scattering characteristic parameters.

Microwave remote sensing can be divided into passive and active forms according to the working principle of remote sensors. Passive microwave systems collect radiation emitted by objects on the ground. In contrast, active microwave systems send out microwave pulses at particular frequencies to interact with ground objects and then measure the backscattered signals. Although passive microwave sensor systems can provide daily observations of snow over a long-time period (Luojus et al., 2021), the generated snow products are only available at coarse spatial resolution (gridded at 25x25 km^2 spatial resolution). These systems cannot provide high spatial-resolution (~100m) observations in mountain areas where the high values of SWE are excluded. Based on these situations, SAR observations have the advantage of providing a wide range of microwave measurements under all-weather conditions at satisfactory spatial resolutions (< 500 m) (Nagler & Rott, 2000). The availability of SAR observations has made it possible to obtain worldwide SAR data with a high spatial resolution of around 10 meters and frequent revisits, typically occurring less than once a week. SAR instruments are predominantly employed in the C-band and have recently been utilized for estimating snow depth in mountainous areas across the northern hemisphere (Lievens et al., 2019). This approach relies on the empirical relationships between SAR observations and ground-based measurements of snow depth and achieve a high retrieval accuracy. However, the approach shows high uncertainty in the comparatively shallow snowpack and non-mountainous regions. Also, the relationships between C-band SAR observations and snow depth are still unclear, and there is uncertainty in explaining this approach physically. Therefore, this work explores the C-band SAR sensitivity to snow accumulation in a non-mountain domain.

Deep learning (DL) algorithms are capable of learning representative and discriminative features from data hierarchically (Zhu et al., 2017) and have recently become a hot spot in machine learning. It has been introduced into the earth science and RS communities for RS extensive data analysis (Zhang et al., 2016). Compared with traditional snow depth retrieval methods based on empirical or semi-empirical relationships, the DL approach can better identify a non-linear relation between multiple inputs and outputs and greatly enhance estimation accuracy. However, the full potential of using DL for parameter estimation from SAR data remains untapped. The majority of remote sensing research has primarily emphasized qualitative issues, as opposed to quantitative challenges that are closely related to computer vision tasks like classification, object detection, segmentation, and noise reduction. (Zhu et al., 2021). In parameter estimation or retrieval, it is important to incorporate a suitable model based on physical principles and approach the problem as regression rather than classification. In this context, having domain-specific knowledge is crucial when utilizing DL techniques, particularly in applications related to the study of snow. Today, there are few studies that apply the DL method in snow mass or SWE estimation from microwave observations (Dai et al., 2011; Paloscia et al., 2008), so the adaptability of deep learning algorithms in data and geographic location needs to be verified.

1.2 Aims and Objectives

The overall aim of this research thesis is to explore the current spaceborne C-band SAR signal sensitivity in the artic tundra snow environment and define a suitable approach for estimating deep snow depth through tundra environment. To fulfill the research goal, these objectives are set below:

- Analyze spaceborne C-band SAR sensitivity on the snow depth in tundra snow environment.

- Test the dominated snow depth retrieval algorithm from C-band observation on the tundra snow environment.

- Explore the deep learning approach capability on tundra snow depth estimation from spaceborne C-band SAR data.

1.3 Thesis Structure

The thesis structure is followed by the University of Waterloo manuscript format where Chapter 3 is formed as a standalone paper and prepared for publishing. In this thesis, Chapter 1 generally introduces the research context, motivation, and objectives across the whole research. Chapter 2 provides related background information on microwave remote sensing in the snow fields, and reviews recent studies regarding monitor or retrieval of snow physical properties from C-band SAR signal. Chapter 3 presents the core manuscript paper entitled "Exploring Radarsat-2 SAR Cross-Polarization Ratio Capability for Tundra Snow Depth Estimation Using Numerical and Deep Learning Approach". Chapter 4 discusses the core findings and summarizes the limitations and future research aims throughout the whole research.

Chapter 2 Research Background

2.1 Basic Principles of Synthetic Aperture Radar

2.1.1 SAR imaging Basic

RADAR (RAdio Detection And Ranging) is an active microwave sensor that can transmit a microwave signal to a target and receive an echo signal. Due to electromagnetic waves propagating through the air at light speed (300,000 km/s), this constant velocity permits the measurement of the travel distance between a reflected object and a radar site by the runtime of the sent pulse. The intensity of the echo signal is used to distinguish between different targets, and the time delay between the transmitted and echo signals is used to detect the distance to the target. The radar equation is a mathematical expression describing the relationship between received echo power, system parameters, and target parameters through a radar system (Woodhouse, 2006), which is expressed as:

$$W_r = \frac{W_t G^2 \lambda^2 \sigma}{(4\pi)^3 R^4} \tag{2.1}$$

Where W_r is the received echo power; W_t is the transmit power; G is the antenna gain; λ is the radar wavelength; σ is the radar cross section of the target; R is the distance between the target and the radar antenna.

With the demand for high spatial resolution, the SAR method was developed when the actual antenna size of the radar could not continue to increase. Usually, a SAR system involves a microwave transmitter, antenna, and receiver. The antenna emits microwave impulses toward the ground, sequentially following the aircraft's flight path. At the same time, the receiver will also receive the echo signal of the same ground object at different flight positions. Finally, relevant demodulation and compression processing will form the SAR imagery. The basic SAR Imaging geometry is illustrated in Figure 2.1.
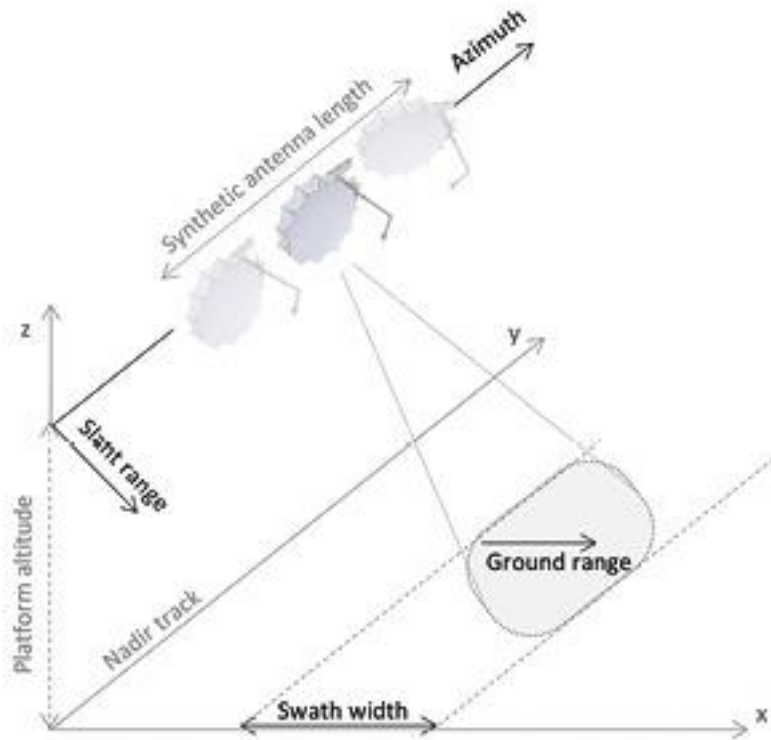
Figure 2. 1 Basic SAR image formation (source: Vekom, 2023)

2.1.2 Frequency

In microwave remote sensing, the most widely used frequencies are from 0.3 GHz to 300 GHz, corresponding to wavelengths from 1 m to 1 mm. The wavelength selected by the radar sensor has a significant influence on what the radar system can achieve. On the one hand, the wavelength determines the depth of penetration of the incident electromagnetic wave and the magnitude of the roughness of the ground surface; on the other hand, the complex dielectric constant of the same feature target is different under different wavelength observations and thus the image characteristics are also different. The commonly used wavelengths for active microwave remote sensing are shown in Figure 2.2. The longer wavelength also has a more vital penetration ability and is less likely to be scattered by the target. When the wavelength is longer than 2 cm, the radar system is no longer affected by clouds.
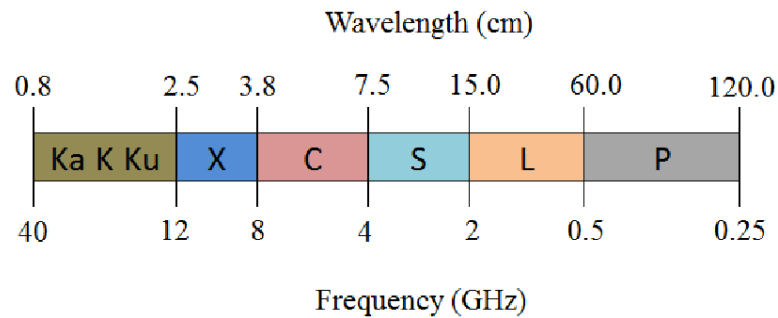
Figure 2. 2 Information of wavelength and frequency used in SAR systems. (Source: Sano et al, 2020)

2.1.3 Resolution

In the SAR system, the dimension of the perpendicular fight direction is called the range, and the dimension of the parallel flight direction is called the azimuth. The spatial resolution of a SAR image includes range resolution and azimuth resolution; usually, the range resolution and azimuth resolution cannot be the same. Since the range resolution depends on the delay of the pulse echo, range resolution is improved by the use of pulse compression, which is related to the bandwidth of the transmitted microwave signal (Figure 2.3). Therefore, a large bandwidth will cause high range resolution, while the azimuth resolution is related to the azimuthal size of the antenna, not to the height of the sensor platform which cannot easily be improved. Note that the spatial resolution of a SAR image gauges how effectively the system can differentiate between nearby targets. Additionally, pixel spacing refers to the gap between neighboring pixels in an image, meaning that a small pixel spacing does not necessarily indicate a high spatial resolution.

Based on the description above, a SAR image has two display forms: slant range and ground range. The slant range represents the measurement of the distance from the SAR sensor to the target, whereas the ground range is the horizontal distance from the target's location on the ground to the point directly beneath the track of sensor. Since the distance on the SAR image is measured by recording the time required for the electromagnetic wave to travel to and from the target, its resolution mode is a slant range. The ground range is the actual distance

between objects on the ground, so before using SAR images to retrieve surface parameters, the slant range resolution must be converted to ground range resolution.
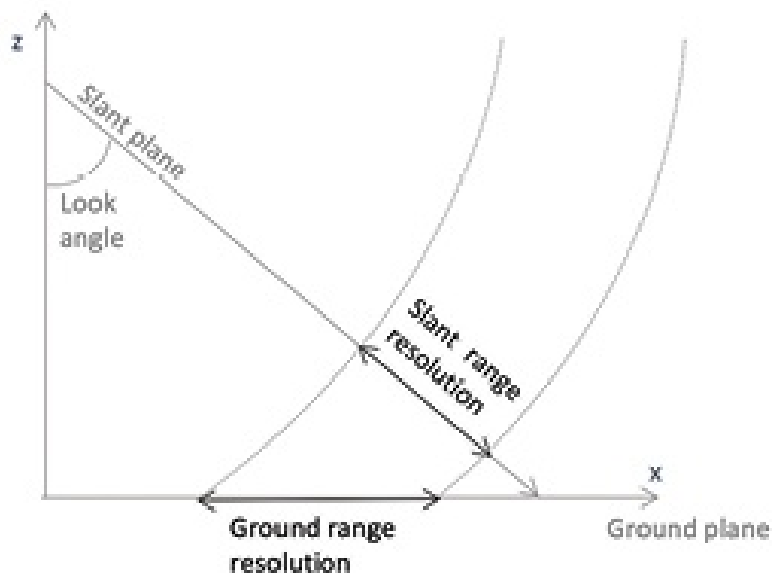
Figure 2. 3 SAR imaging resolution (source: Vekom, 2023)

2.1.4 Incident angle and Local incident angle

In radar observation, the incidence angle is the angle between the radar incident beam and the normal of the local geoid. The radar incidence angle is aimed at the ideal flat ground. However, when the ground surface is more undulating, it is necessary to consider the role of the radar beam and the local terrain, which gives rise to the concept of local incidence angle. The local incidence angle can be defined as the angle between the radar incident beam and the surface typical of the local terrain, which fully considers the effect of the local terrain on the radar signal. Figure 2.4 shows the relation between the incident angle and the local incident angle. Since the interaction of microwaves with the ground surface is complex, different angles will produce different reflections and scattering. A larger incidence angle generally achieves better image swath ground coverage. However, it increases the path of microwave propagation and the amount of ground features penetrated, weakening the strength of the return signal. In

contrast, a smaller incidence angle usually shortens the propagation path, reduces target scattering and returns a stronger signal.
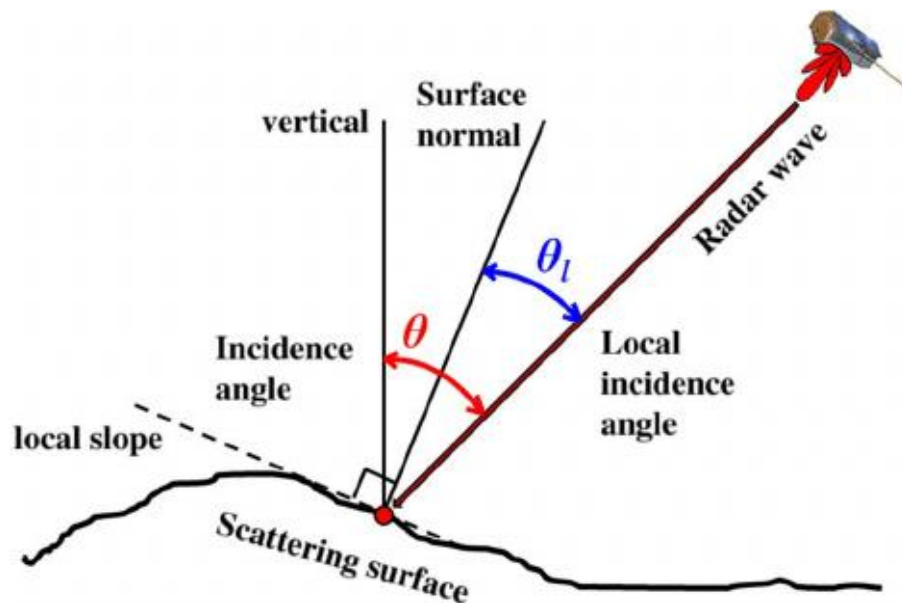
Figure 2. 4 incident angle (red) and local incident angle (blue) (Rizzoli & Bräutigam, 2014)

2.1.5 Polarization

Polarization is defined as the vector direction of electromagnetic wave vibration, and the most basic is divided into horizontal polarization and vertical polarization. There are four kinds of polarization modes commonly used in radar remote sensing systems: HH, VV, HV, and VH. The first two (HH and VV) indicate that the incident electromagnetic wave and the return electromagnetic wave have the same propagation mode, which is called the same polarization, and the latter two (HV and VH) indicate the incident electromagnetic wave and the return electromagnetic wave. The returning electromagnetic waves have a different way of propagating, called opposite (crossed) polarizations. Compared with the cross-polarization method, the backscattering coefficients and characteristics of surface objects are different under the action of horizontal and vertical polarization waves or the combination of different polarization methods. Therefore, in addition to increasing the remote sensing the valuable information from different polarizations could also improve the accuracy of target recognition.

11

Figure 2.5 is a schematic diagram of vertical and horizontal polarization of electromagnetic waves:
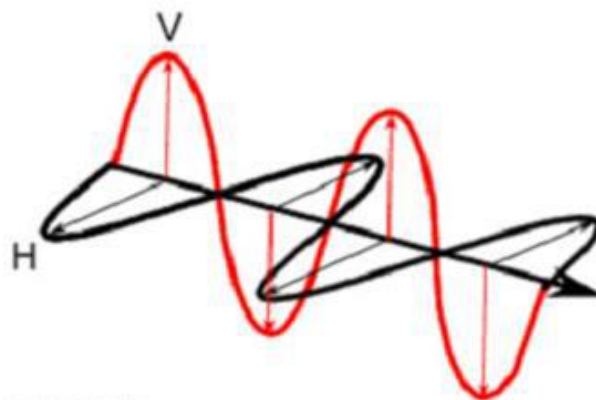
Figure 2. 5 H (Horizontal) and V (Vertical) polarizations of the electromagnetic wave (Source: Natural Resources Canada, 2018)

2.1.6 Backscattering coefficient

The radar backscatter coefficient is defined as the reflectivity of the radar per unit cross-sectional area or the radar scattering interface per unit illuminated area, which is used to measure the result of the interaction between the incident wave and the target. In microwave remote sensing, the scattering intensity in the incident direction or the average radar scattering cross section per unit area of the target is called the backscatter coefficient (σ^0), and its unit is the decibel (dB), which is expressed as below:

$$\sigma^0 = \frac{\sigma}{A} \tag{2.2}$$

Where: σ is the radar scattering cross section; A is the effective illuminated area of the radar beam.

In the SAR image, the raw data signals received by the SAR sensor are a complex number with a real part and an imaginary part. However, the raw data could not be used directly and needed to be processed in SLC (single look complex) form, the first level images transformed from the raw signals. However, the SLC image only contains the microwave phase information I (in-phase) and Q (quadrature) in complex number format. However, human eye

could not make interpretation of the SLC image from either I and Q images, so the complex values of I and Q need to be converted to the intensity that represents to the DN (digital number) value; the equation is shown as:

$$DN = \sqrt{(I)^2 + (Q)^2} \tag{2.3}$$

After that, radiometric calibration is fundamental to generating the backscatter coefficient information for different objects. Three geocoded backscatter coefficients can be obtained in the radiometric calibration that contains different information. Firstly, the radar brightness coefficient (β^0) represents the reflectivity in slant range geometry, that can be calculated as:

$$\beta^0 = \frac{DN^2}{A^2} \tag{2.4}$$

where DN refers to the calculated digital number and A^2 is the scaling gain value from the Look Up Tables (LUTs). Based on the calculated β^0 value, the radar backscatter coefficient (σ^0) represents the strength of radar signals reflected by a distributed scatterer, which is calculated as:

$$\sigma^0 = \beta^0 * \sin(\theta) \tag{2.5}$$

Also, the Gamma backscatter coefficient (γ) refer to the backscattering coefficient normalized by the cosine of the incidence angle (θ), which is shown as below:

$$\gamma^0 = \beta^0 * \cos(\theta) \tag{2.6}$$

Notice, the intensity of the radar backscattering coefficient depends on the following two types of factors:

- SAR system parameters - wavelength (frequency), incident angle, polarization mode

- Target characteristic parameters - dielectric constant, surface roughness, slope, shape, local incidence angle.

Changes in any of these parameters may affect changes in backscattered intensity of SAR.

2.2 Snowpack Scattering Mechanisms from SAR

In electromagnetic propagation of microwave, the relative permittivity (also called dielectric constant) is used to quantify physical scattering properties of different materials (Woodhouse, 2006). Usually, snowpack comes in both dry and wet forms in nature. Dry snow consists of ice crystals and air, while wet snow is a combination of ice crystals, air, and liquid water. The dielectric constants at 0°C are 1 for air, 3.15 for pure ice, and 80 for water. (Hallikainen, 1977). Dry snow has a low permittivity that cannot efficiently conduct electric current. Nonetheless, the presence of liquid water can result in significant dielectric loss, causing the wet snowpack to absorb more microwave energy and reducing the depth to which microwaves penetrate (Rott et al. 1988; Shi & Dozier, 1997). Additionally, various physical characteristics of the snowpack, such as snow density, grain size, and temperature, have the potential to affect the dielectric properties of the snow (Chang et al., 1982; Rosenfeld 2000). The depth to which a microwave signal can penetrate not only relies on the dielectric properties of the snowpack but also on the frequency of the radar signal itself. Different frequencies lead to distinct scattering interactions within the snowpack. Generally, lower frequency (longer wavelength) has an extended penetration depth. without wet snow, L-band or C-band can usually penetrate through a seasonal dry snowpack, the radar signal will not be influenced within the snowpack, so the backscatter at these frequencies will mainly come from the ground. At higher frequencies (shorter wavelengths) such as Ku- and Ka-band, the backscatter will be dominated by the snow volume scattering.

To understand the scattering mechanism of snow, Figure 2.6 shows the basic four-components model from Rott et al. (2010), which was widely used to model SAR observed total backscatter (σ_{pq}^{total}) over a pure snowpack on bare soil with the different polarization mode, the physical formula was summarized below:

$$\sigma_{pq}^{total} = \sigma_{pq}^{air-snow} + \sigma_{pq}^{snowvol} + \sigma_{pq}^{snowvol-gmd} + \sigma_{pq}^{gmd} * e^{(-\frac{2\tau_p}{cos\theta})} \qquad (2.7)$$

where p and q refer to the H and V polarization mode, such as σ_{VH} represents backscatter emitted at H polarization and received at V polarization. $\sigma_{pq}^{air-snow}$ is the scattering from the

air–snow interface, which can be neglected except for wet snow due to the low permittivity contrast between air and snow (Rott et al., 2010). The $\sigma_{pq}^{snowvol}$ is the volume scattering from the snowpack that related snow microstructure such as thickness, snow density, grain size, snow layering. $\sigma_{pq}^{snowvol-gmd}$ is the higher order scattering between the snow volume and ground surface. $\sigma_{pq}^{gmd} * e^{(-\frac{2\tau_p}{cos\theta})}$ is the scattering from the underlying rough soil surface and attenuated by the snow layer through $e^{(-\frac{2\tau_p}{cos\theta})}$, and the amount of attenuation depends on the optical thickness of the snowpack (τ_p) and the radar incidence angle (θ). At C-band, the total backscatter of dry snow will be from the snow volume scattering and ground surface scattering. When the dry snow becomes wet, the total radar backscatter will mainly come from a surface scattering of air-snow interface and any volume scattering from dry snow.
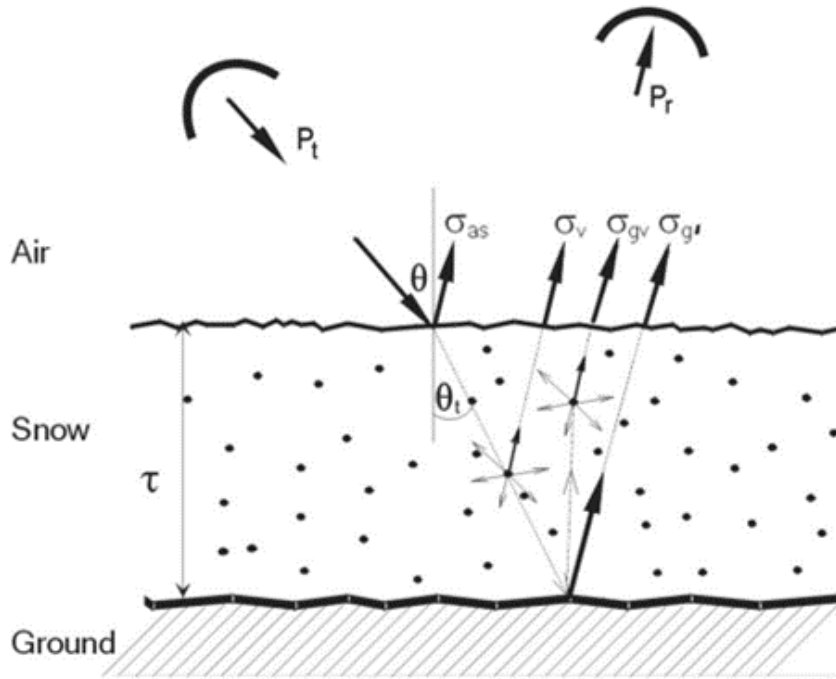
Figure 2. 6 Four components model of SAR observed total backscatter on snowpack (Source: Rott et al., 2010)

2.3 Snow studies from C-band SAR backscatter

2.3.1 Wet snow

Based on the above description of scattering mechanisms in different snow types, the penetration depth decreases when the liquid water content increases, which means the low-frequency microwave is more suitable for distinguishing wet snow and dry snow. Earlier studies have found that dry snow is generally shown as transparent and less different from bare ground for C-band observations. In contrast, wet snow shows more significant backscatter variability due to the high dielectric constant of water with non-wet snow surfaces (Matzler & Schanda, 1984; Rott & Nagler, 1993). In the early 1990s, as C-band SAR satellite systems could provide more repeated and rapid image products, C-band was considered the excellent microwave frequency for detecting wet snow (Rott & Nagler, 1993). Thus, Rott and Nagler (1993) developed a wet snow detection method from the C-band SAR multi-temporal images based on a change detection method using the image ratio between non-wet snow reference and wet snow. Also, the -3 dB threshold was proposed by the physically based models and experimental tests of aircraft SAR systems; any image ratio less than -3 dB will be identified as wet snow. Furthermore, Nagler and Rott (2000) enhanced the initial change detection technique for a mountainous region by incorporating the average value of multiple reference images. This modification was aimed at mitigating the impact of environmental factors on co-polarized backscattering. They switched the threshold to -2 dB in mountain ranges. More recently, the Nagler algorithm became a widely used wet snow detection method due to its relatively simple implementation and high detection accuracy in most experiments (Tsai, et al. 2019). With the C-band SAR development, Nagler et al. (2016) found that dual-polarized observations could achieve higher classification accuracies than single polarization on wet snow mapping.

2.3.2 Dry snow

In the early 1990s, the lack of dual-polarized and full-polarized observations at C-band SAR meant that most snow studies focused on wet snow detection research with single-

polarization such as HH or VV. In essence, C-band SAR was assumed not to be sensitive to dry snow, and only a few studies focused on the cross-polarization observations to dry snowpack. With the development of C-band SAR systems such as Radarsat-2 and Sentinel-1, high spatial resolution, frequent revisits, and multi-polarization SAR observations provided more opportunities for dry snow studies. Based on the open-source Sentinel-1 SAR data, Lievens et al. (2019) found that the cross-pol (VH) backscatter gradually increases with the accumulation of (dry) snow during the winter, while co-pol (VV) backscatter remains relatively constant with dry snow and mainly from the ground surface condition. Thus, the ratio of cross- to co-pol backscatter (also called cross-polarization ratio) could partially eliminate the effects of the ground surface, vegetation, or snow conditions and enhance the sensitivity of cross-pol to snow depth. Detailed results of the cross-polarization ratio approach are shown in Figure 2.7.
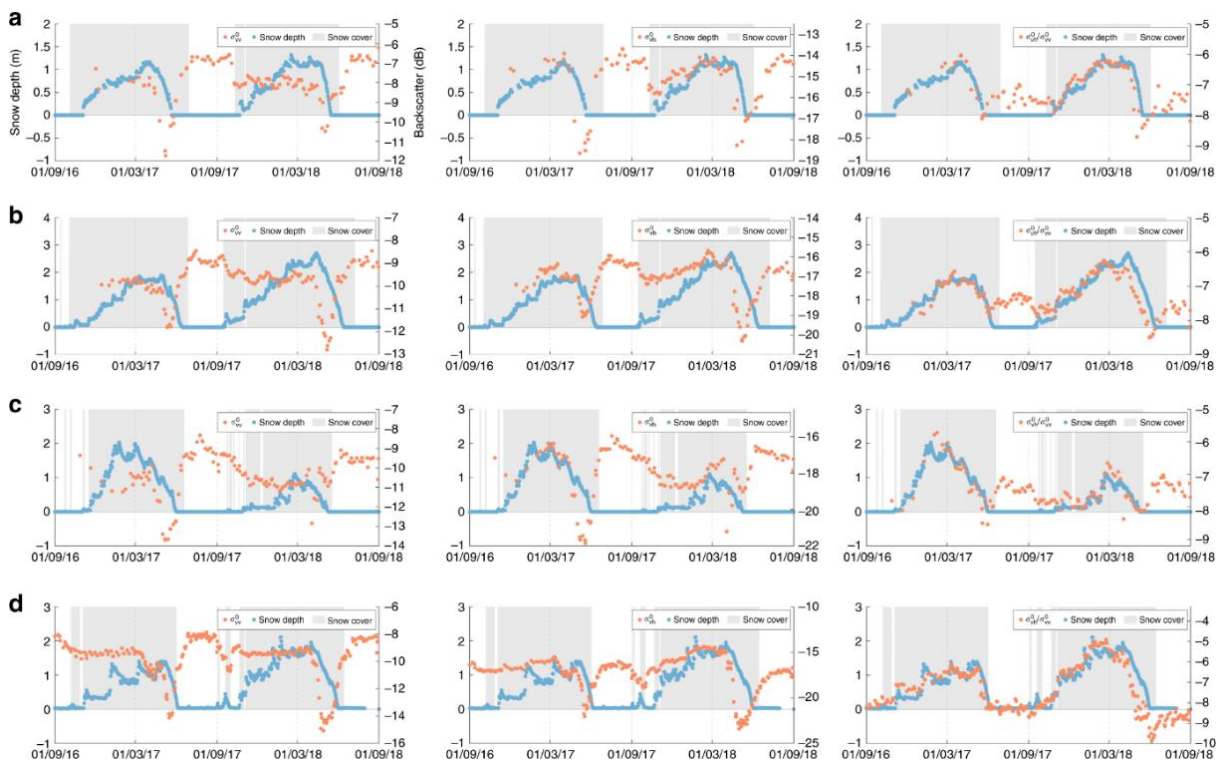
Figure 2. 7 Time series of co-pol backscatter (left column), cross-pol backscatter (middle column), cross-polarization ratio (right column) and snow depth at 4 sites. (a) Omineca Mountains, (b) Absaroka Range, (c) San Juan Mountains, (d) European Alps (Source: Lievens et al. (2019))

17

With the high spatial and temporal correlation between CPR (cross-polarization ratio) and snow depth, Lievens et al. (2019) developed the CPR-based empirical change detection algorithm that was used to estimate mountain snow depth at 1 km spatial resolution from the C-band (Sentinel-1) observations across the northern hemisphere, while also achieving the relatively high retrieval accuracy (~0.8 correlation and 0.27m mean average error, or MAE) compared with in-situ measurement. Since Lievens approach is based on the hypothesis of spatial-temporal correlation between C-band CPR value and snow depth, the sensitivity still needs to be validated from more snow depth samples under different environments. Even though the high retrieval accuracy in the whole range of snow depth is achieved from the algorithm, a large MAE exists within the shallow snow depth area, which means the approach is applicable only to deep snow (over 1 m). Furthermore, the proposed approach is calculated from Sentinel-1 SAR observation at lower spatial resolution, which may lose more detailed snow depth variation. Moreover, the adjusted parameters are based on regional station observations; improvements to the parameters could be achieved with more snow depth observations. More recently, Lievens et al. (2022) improved the change detection algorithm by combining CPR and co-pol backscatter values, which could estimate snow depth at sub-kilometer resolution over the European Alps. While Lievens et al. (2019) found limited sensitivity of co-pol backscatter to dry snow accumulation in mountains, the improved algorithm (Lievens et al., 2022) shows co-pol sensitivity to snow thickness increases in forest area of the Alps. This discrepancy raises concerns about the generalizability of the improved approach to different geographical settings, and the sensitivity of co-pol backscatter under forest areas still needs to be further assessed.

2.4 Neural network potential on SAR Remote Sensing

With the rapid development of AI (artificial intelligence), deep learning (DL) algorithms can learn representative and discriminative features from data hierarchically (Zhu et al., 2017). DL has recently become a focus in machine learning and has been introduced into the earth science and RS communities for RS extensive data analysis (Zhang et al., 2016). Unlike conventional algorithms, deep learning-based methods, such as deep neural networks,

can extract target features from the raw data with multiple hierarchical architectures; the extracted features can be applied to numerous tasks such as image recognition, object detection, and semantic segmentation (Zhang et al., 2021). When deep learning is applied to SAR image data, various applications have been successfully demonstrated including terrain surface classification (Parikh, et al. ,2020), object detection (Chen & Wang, 2014), despeckling (Wang et al., 2017), interferometric SAR (InSAR) (Anantrasirichai et al., 2018), and SAR–optical data fusion (Hughes et al., 2018). Beyond these applications, the parameter inversion from SAR images is a challenging field. Several studies show the improved performance of neural network in estimating snow depth (Santi et al, 2021) from SAR observations. In conclusion, this emerging field provides opportunities to explore and verify the applicability and feasibility of deep learning algorithms in snow depth estimation from C-band SAR observation.

In conclusion, the knowledge gap exists between C-band SAR sensitivity on dry snow. The current snow depth retrieval still needs testing on other areas with shallow to deep snow. However, deep learning provides another way to estimate snow depth in tundra snow environments from C-band SAR observations. Therefore, this study aims to explore the C-band SAR sensitivity on tundra snow and find a better approach to estimate snow depth from C-band SAR.

Chapter 3 Exploring Radarsat-2 SAR Cross-Polarization Ratio Capability on Tundra Snow Depth Estimation from Numerical and Deep learning approach

3.1 Introduction

Seasonal snow cover, which blankets approximately 47 million square kilometers of the Earth's surface annually (constituting 31% of the land area), is the most extensively varying surface feature in the northern hemisphere. It serves as a vital indicator and influencer of the Earth's climate system. Notably, in recent times, the decline in Northern Hemisphere spring snow cover has occurred at a rate roughly comparable to that of the reduction in Arctic summer sea ice, around 13% per decade (Tsang et al., 2022). A significant portion of the global population, exceeding one-sixth, depends on seasonal snowpacks and glaciers as a source of freshwater augmentation. However, it is anticipated that this source is poised to diminish in the coming century (Barnett et al., 2015). Snow is also a critical component of Earth's radiation balance. Snow plays a pivotal role in maintaining Earth's radiation equilibrium. The 2018 Special Report on the Ocean and Cryosphere in a Changing Climate from the Intergovernmental Panel on Climate Change (IPCC) underscored the significant dangers associated with heightened snow variability and accelerated melting, stemming from global warming.

Despite its importance, snow mass (expressed as snow water equivalent or SWE) is poorly observed in the vast northern hemisphere snow extent (Tsang et al., 2022). Due to the need for more stable and denser hydrological and meteorological station networks, large-scale SWE monitoring has a high degree of uncertainty (Li et al., 2020). Manual snow surveys can offer precise measurements of SWE, but it is labor-intensive and costly, notably in comparison to automated snow measurements (Sturm et al., 2010; Odry et al., 2020). Therefore, satellite RS technology has the advantages of macroscopic, rapid, multi-temporal, and multi-frequency snow monitoring. In areas with insufficient meteorological data and harsh climatic conditions, RS is a viable method that can reflect the status and changes of large-scale snow cover (Foster et al., 2011). However, visible-infrared satellite imagery acquired for snow cover extent

20

estimates is applicable only under cloud-free conditions and does not support the retrieval/estimation of SWE. Therefore, passive or active microwave remote sensing is widely used in snowpack studies due to its advantage of frequent measurements of the Earth under most weather conditions (except heavy precipitation), whether day or night.

While passive microwave measurements have the potential to offer extended time series of snow mass data (Luojus et al., 2021), the limitations of coarse spatial resolution (25 x 25 km) and bias on shallow to moderately deep snow make it challenging to measure deep snow at high spital resolution (Pulliainen et al., 2020). Active microwave assessments exhibit significant potential for accurately retrieving SWE with fine spatial detail. Radar systems typically operate within the frequency range spanning from the Ka-band to the P-band. X- and Ku- bands have a distinctive scattering within the snow volume (Yueh et al., 2009; King et al., 2015), These systems offer valuable insights into fluctuations in SWE, the microstructure of snow, and whether the snow is wet or dry. Moreover, the European Space Agency Cold Regions Hydrology High-Resolution Observatory (CoReH2O) mission proposal, equipped with dual-frequency X- and Ku-band radar, served as a substantial driving force in this context (Rott et al., 2010). Hence, the optimal frequencies for monitoring snow cover on a global scale are expected to fall within the range of approximately 8 to 18 GHz. Regrettably, high-resolution satellite observations in the Ku or Ka bands have not been accessible worldwide until recently.

Recently, open-sourced spaceborne SAR backscatter data with a fine spatial resolution and frequent revisits, are solely provided at the C-band frequency. Even though these regular observations are readily accessible, there has been a lack of focus on harnessing C-band backscatter for snow monitoring, primarily because earlier satellite observations had indicated its limited sensitivity on dry snow. (Bernier et al., 1999; Shi & Dozier, 2000). In 2019, Lievens et al. (2019) discovered how Sentinel-1 SAR cross-polarization ratio (CPR) measurements are responsive to the accumulation of dry snow during the winter season. They devised an approach employing an empirical change detection algorithm to estimate snow depth at a spatial resolution of 1 kilometer for all mountainous regions in the Northern Hemisphere. Their findings indicate a strong temporal correlation between the CPR backscatter and snow depth.

While the physical mechanism driving this approach have not been fully defined, Lievens et al. (2019) suggested that as the thickness of the snowpack increases, the path length of the C-band signal through the snow increases, which could increase the opportunities for scattering in snow volume. The study notes that the approach is valid for deeper snow (more than 50 cm) at C-band. However, it is unknown whether the proposed approach might work for other cases of deep snow in non-mountainous terrain, such as deep drifted gulley in the tundra.

Machine Learning (ML) currently offers a viable strategy for tackling challenges characterized by incomplete theoretical understanding but abundant observational data (Müller & Guido, 2016). The snow depth retrieval problem from C-band SAR represents a good application example. Due to the escalating computational capabilities of modern computers, Deep Learning (DL), and Neural Networks (NN) in particular, have garnered significantly heightened attention as powerful tools for addressing a diverse array of non-linear problems (Ma et al., 2019). In contrast to other ML methods, NN have demonstrated the capacity to provide a favorable balance between retrieval accuracy and computational expenses (Paloscia et al., 2008). There are an increasingly number of studies showing NN potential for the retrieval of surface parameters from SAR and microwave radiometers (Dai et al., 2011; Paloscia et al., 2008). Currently, the research of Santi et al. (2021) shows the high capability of neural networks in snow depth estimation by using X- and Ku-band SAR data. Further, the validation of trained model resulted in a 0.77 correlation coefficient between estimated and target SD with 0.13 m root-mean-square error (RMSE). However, this emerging field provides opportunities to explore and verify the applicability and feasibility of deep learning algorithms in snow depth estimation from C-band SAR observation.

In this study, the general goal is to evaluate the empirical CPR method of Lievens using high spatial resolution Radarsat-2 data. Given the nature of the empirical approach, the aim is to compare the cross-polarization-ratio method in estimating snow depth with a non-linear machine/deep learning approach. The three objectives are specified thus:

1. Evaluate the CPR method's sensitivity to deep tundra snow for different surface vegetation and topography, using Radarsat-2 SAR observations.

2. Apply and adapt the snow depth retrieval algorithm from Lievens et al. (2019) to tundra snow at a higher spatial resolution.

3. Develop and evaluate a deep learning-based snow depth estimation model with the C-band SAR data and compare it with the empirical CPR method.

In the following sections, the study area is introduced in Section 3.2, the datasets used in this study are described in Section 3.3, including the SAR dataset, airborne-based snow depth data, ground-based measurements, vegetation class map, digital terrain model and vegetation height map. Section 3.4 presents the methodology, details of sensitivity analysis and implementation of numerical and deep learning approaches on snow depth estimation. Then, the results of the analysis and estimation are presented and discussed in Section 3.5 and Section 3.6. And lastly, Section 3.7 states the main conclusions and findings though the whole chapter.

3.2 Study Area

The investigation conducted in this study relied predominantly on data acquired from the Trail Valley Creek (TVC), spanning September 2017 to June 2019. The TVC is geographically situated approximately 50 kilometers north of Inuvik, within the Northwest Territories of Canada (shown in Figure 3.1). The TVC basin, encompassing an area of approximately 58 km^2, features watersheds that ultimately contribute to the Husky Lake estuary network. Significantly, the basin exhibits continuous ice-rich permafrost, characterized by an active layer thickness ranging from 0.3 to 1 m (Trail Valley Creek Arctic Research Station, 2023). The climatic conditions prevailing in this locale are defined by abbreviated summer seasons and prolonged, frigid winters, marked by a protracted snow cover persisting for eight months (Pomeroy et al., 1997). The mean annual air temperature is approximately -8.2 °C, with an annual snow precipitation of about 159 cm (Environment Canada, 2016). Empirical observations substantiate that the principal determinants influencing snow depth distribution at TVC are the local topography and vegetation density (Sturm and Benson, 2004; Pohl and Marsh, 2006; Derksen et al., 2009). Additionally, a considerable accumulation of

snow occurs in expansive hillslopes and channel drifts during the late winter period, manifesting depths ranging from 0.1 to 4 m (Walker et al., 2020).
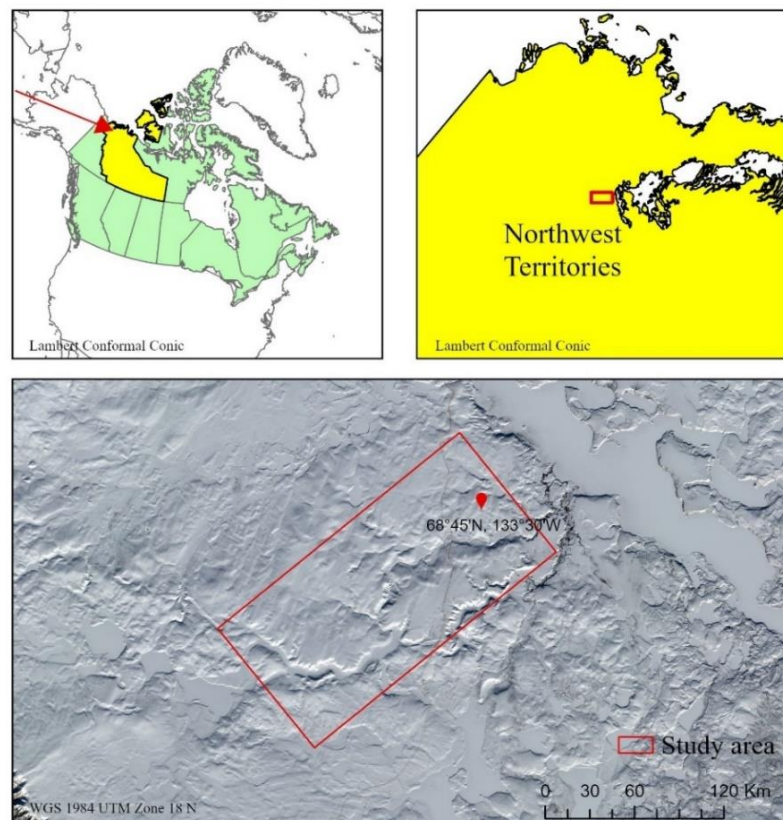
Figure 3. 1 The location of the TVC and extent of the Study area in Northwest Territories, Canada. Source of imagery: Sentinel-2 in 2018 03-11

As elucidated by Boike et al. (2019), the research site under consideration encompasses six principal vegetation categories: trees, tall shrubs, riparian shrubs, dwarf shrubs, tussocks, and lichens. Among these, tussocks, lichens, and dwarf shrubs exhibit greater prevalence, while trees and tall shrubs are comparatively less abundant. In terms of terrain characteristics, the study area is distinguished by mineral soil hummocks, some of which attain diameters of up to one meter, juxtaposed with peaty inter-hummock depressions (Quinton and Marsh, 1998). Furthermore, the southern periphery of the research site manifests heightened topographic intricacies, particularly in proximity to forested regions. The presence of numerous lakes,

streams, and rivers within the study area contributes to the observable clustering of trees, tall shrubs, and riparian shrubs along watercourses, especially within drifts and gullies.

In accordance with the investigations conducted by Dutch et al. (2022), a comprehensive array of meteorological and soil moisture measurements was made at the TVC research site spanning the duration of 2017 to 2019. This encompassed meticulous recordings of daily averaged air temperature, precipitation, as well as soil temperature and soil water content at depths of 5cm and 20cm, as visually represented in Figure 3.2. The air temperature consistently maintained sub-freezing conditions during the periods spanning October 2017 to May 2018 and September 2018 to May 2019. Additionally, the initiation of the snowpack occurred in October 2017 and September 2018, respectively. Consequently, it is postulated that the snowpack assumed a characteristic of dry snow, constituting a composite of ice and air, throughout the entirety of TVC study site during the subfreezing intervals. Simultaneously, soil freezing commencement correlated with the onset of snowfall, with the soil temperature exhibiting a decreasing trajectory during the presence of the snowpack, irrespective of the depth of soil layer, be it 20 cm or 5 cm.
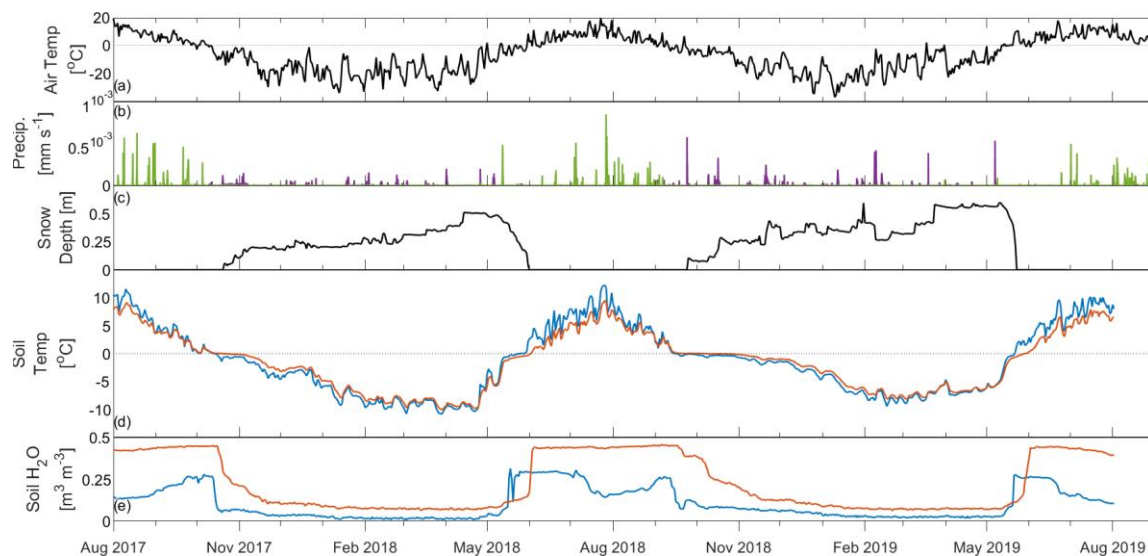
Figure 3. 2 Daily meteorological and soil information at TVC from 2017 August to 2019 August: (a) air temperature, (b) snowfall (purple) and rain (green), (c) snow depth, (d) soil temperatures at depths of 5 cm (blue) and 20 cm (orange), and (e) volumetric soil water content at 5 cm (blue) and 20 cm (orange) depths. (Source: Dutch et al. (2022))

3.3 Datasets

3.3.1 RADARSAT-2 SAR data

Launched on December 14, 2007, the RADARSAT-2 (RSAT-2) SAR satellite represents a significant advancement in high-resolution commercial radar technology, incorporating a C-band (5.406 GHz) SAR instrument. This satellite, a collaborative venture between the Canadian Space Agency (CSA) and MacDonald Dettwiler and Associates Ltd (MDA), succeeded RADARSAT-1 satellite. Conceived with an operational lifespan ranging from 7 to 12 years, RSAT-2 continues to orbit the Earth today. RSAT-2 has augmented capabilities, permitting the dynamic switching of all its beams between left-view and right-view configurations upon command issuance. This feature translates to reduced revisit times and an enhanced capacity for acquiring stereoscopic images. Furthermore, RSAT-2 preserves the imaging modes of RADARSAT-1 while introducing additional modalities, including spotlight mode, super fine mode, quad-polarization (encompassing standard, wide standard, fine, wide fine), and multi-fine mode. An instrumental facet of the RSAT-2 SAR sensor lies in its capacity to transmit and receive signals polarized both horizontally (H) and vertically (V). This dual-polarization capability facilitates the generation of quad-polarization products, concurrently furnishing vertical–vertical (VV), vertical-horizontal (VH), horizontal-horizontal (HH), and horizontal-vertical (HV) data, alongside inter-channel phase information.

The used RSAT-2 SAR data employed in this study comprises SLC products of the FQ19W (Wide Fine Quad Polarization 19 Beam Mode) acquired during ascending orbital passes. This data product affords full polarimetric imaging (HH+VV+HV+VH) at a nominal spatial resolution of 5 m (range direction) $\times$ 8 m (azimuth direction) and an extended swath coverage of approximately 25 x 50 km, offering a revisit time of 24 days. Additionally, the antenna beam's incident angle spans from 37 to 40 degrees across the near to far range. As detailed in the product documentation by MDA (MDA, 2018), the Noise-Equivalent Sigma-Zero (NESZ) of the FQ19W data mode is estimated to be approximately -33 dB. In the context of this research, a total of 18 scenes were identified, specifically during winter periods spanning 2017 to 2019. The acquisition dates are meticulously cataloged in Table 3.1.

Table 3. 1 Summary of used RSAT-2 product name, acquisition dates, beam modes, polarizations, and pass orbits at within TVC range.

Product name	Acquisition dates	Beam mode	Polarization	Pass Orbits
RS2_OK90251_PK799256_DK727468_FQ19W _20170928_022237_HH_VV_HV_VH_SLC	2017-09-28	FQ19W	HH VV VH HV	Ascending
RS2_OK91173_PK806321_DK737477_FQ19W _20171022_022236_HH_VV_HV_VH_SLC	2017-10-22	FQ19W	HH VV VH HV	Ascending
RS2_OK91944_PK812848_DK741171_FQ19W _20171115_022234_HH_VV_HV_VH_SLC	2017-11-15	FQ19W	HH VV VH HV	Ascending
RS2_OK92790_PK820009_DK748135_FQ19W _20171209_022232_HH_VV_HV_VH_SLC	2017-12-09	FQ19W	HH VV VH HV	Ascending
RS2_OK93404_PK824819_DK754420_FQ19W _20180102_022229_HH_VV_HV_VH_SLC	2018-01-02	FQ19W	HH VV VH HV	Ascending
RS2_OK93406_PK824938_DK754539_FQ19W _20180126_022226_HH_VV_HV_VH_SLC	2018-01-26	FQ19W	HH VV VH HV	Ascending
RS2_OK94440_PK832102_DK763268_FQ19W _20180219_022224_HH_VV_HV_VH_SLC	2018-02-19	FQ19W	HH VV VH HV	Ascending
RS2_OK95250_PK837907_DK768984_FQ19W _20180315_022223_HH_VV_HV_VH_SLC	2018-03-15	FQ19W	HH VV VH HV	Ascending
RS2_OK96228_PK845567_DK776989_FQ19W _20180408_022222_HH_VV_HV_VH_SLC	2018-04-08	FQ19W	HH VV VH HV	Ascending
RS2_OK101006_PK877104_DK810439_FQ19W _20180923_022216_HH_VV_HV_VH_SLC	2018-09-23	FQ19W	HH VV VH HV	Ascending
RS2_OK101930_PK882793_DK815839_FQ19W _20181017_022215_HH_VV_HV_VH_SLC	2018-10-17	FQ19W	HH VV VH HV	Ascending
RS2_OK102869_PK890647_DK824128_FQ19W _20181110_022210_HH_VV_HV_VH_SLC	2018-11-10	FQ19W	HH VV VH HV	Ascending
RS2_OK103534_PK898725_DK832564_FQ19W _20181204_022208_HH_VV_HV_VH_SLC	2018-12-04	FQ19W	HH VV VH HV	Ascending
RS2_OK103535_PK898791_DK832630_FQ19W _20181228_022204_HH_VV_HV_VH_SLC	2018-12-28	FQ19W	HH VV VH HV	Ascending
RS2_OK104518_PK906406_DK839417_FQ19W _20190121_022205_HH_VV_HV_VH_SLC	2019-01-21	FQ19W	HH VV VH HV	Ascending
RS2_OK105434_PK917704_DK850012_FQ19W _20190214_022203_HH_VV_HV_VH_SLC	2019-02-14	FQ19W	HH VV VH HV	Ascending
RS2_OK106934_PK932025_DK866896_FQ19W _20190310_022201_HH_VV_HV_VH_SLC	2019-03-10	FQ19W	HH VV VH HV	Ascending
RS2_OK107832_PK939911_DK876160_FQ19W _20190403_022201_HH_VV_HV_VH_SLC	2019-04-03	FQ19W	HH VV VH HV	Ascending

3.3.2 TVC Drone-based Snow depth data

Conventional techniques for assessing snowpack depth have encountered limitations in accurately capturing depth information, particularly in areas characterized by deep drifts or gullies. Consequently, there has been a paradigm shift towards the adoption of drone-based methodologies, offering the distinct advantage of providing high-resolution, spatially distributed, and precise snow depth data across the watershed. Technically, the computation of drone-based snow depth entails the derivation of the difference between two elevation datasets: a Digital Elevation Model (DEM) representing the snow surface elevation and another representing the terrain elevation devoid of snow. This calculation is formally expressed as:

$$\text{SD} = DEM_{snow-on} - DEM_{snow-free} \text{ (meter)} \tag{3.1}$$

During the experimental period spanning 2018 to 2019, two distinct drone-based snow depth datasets were employed as reference data, as described in the studies conducted by Wang et al. (2022) and Walker et al. (2020). The drone-based snow depth data location and acquisition date are shown in Figure 3.3. Both datasets are characterized as raster products and feature a spatial resolution of 1 meter georeferenced to the WGS 1984/ UTM zone 8N projection. The snow depth products presented by Walker et al. (2020) were generated across seven Areas of Interest (AOIs) through the disparity between a snow-on digital surface model derived through Structure-from-Motion (SfM) photogrammetry, and a snow-free bare-ground LiDAR (Light Detection and Ranging) DEM from 2008 (Hopkinson et al., 2008), specifically during March to April 2018. The evaluation of these snow depth products against in-situ measurements (7191 samples) yielded a mean RMSE of 0.15 m. In the case of the snow depth dataset presented by Wang et al. (2022), the snow depth product for April 10, 2019, was computed by juxtaposing a snow-on DEM derived from Airborne Laser Scanning (ALS) point cloud data with a snow-free LiDAR Digital Terrain Model (DTM) produced in 2016 (Anders et al., 2018). The validation process involved an estimated RMSE of 0.16 m, validated against 4334 field snow depth measurements encompassing various vegetation types. The collective evaluation of these datasets underscores the high fidelity of drone-based snow depth data, affirming its capacity to offer high resolution, extensive spatial coverage, and minimal errors,

rendering it suitable as reference data for assessing the sensitivity of C-band SAR in tundra snow environments.
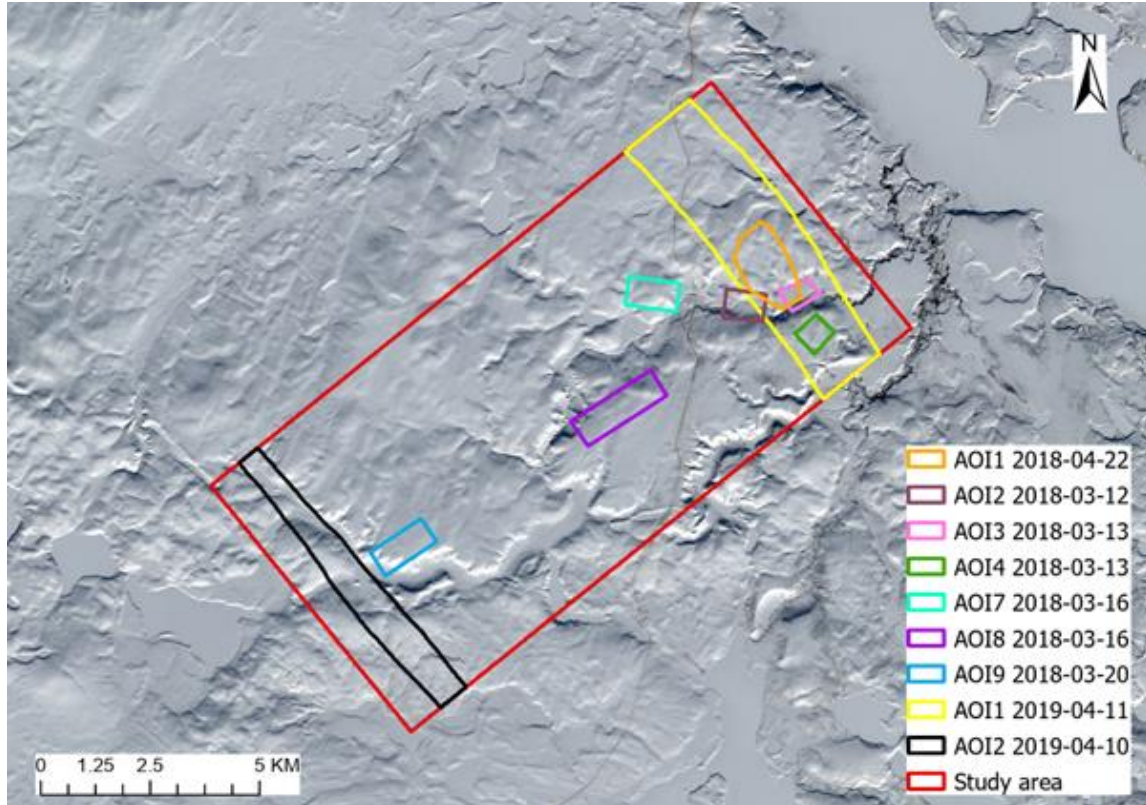
Figure 3. 3 Drone-based snow depth areas of interest (AOI) from 2018 to 2019.

3.3.3 TVC Vegetation class map

To assess the influence of underlying vegetation on the backscattering signal received from the snowpack, a vegetation class distribution map was used. This map elucidates how distinct vegetation types modulate RSAT-2 backscatter across varying polarization states. For the TVC study area, a meticulously crafted vegetation class map is at our disposal, courtesy of Boike et al. (2019). This map has undergone conversion into a raster format with a spatial resolution of 10 meters and has been georeferenced to the WGS 84/UTM zone 8N coordinate system. The vegetation map classifies vegetation into six distinct categories: trees, tall shrubs, riparian shrubs, dwarf shrubs, tussocks, and lichen, as visually depicted in Figure 3.4. Boike et al. (2019) formulated this vegetation class map through the integration of ALS point cloud data

and airborne orthophotos, achieving a classification accuracy of 87.7% for the validation dataset and 89.5% for the calibration dataset. It is imperative to acknowledge that certain grid cells may encompass a blend of diverse vegetation types within the 10-meter resolution, particularly evident in the case of tall shrubs.
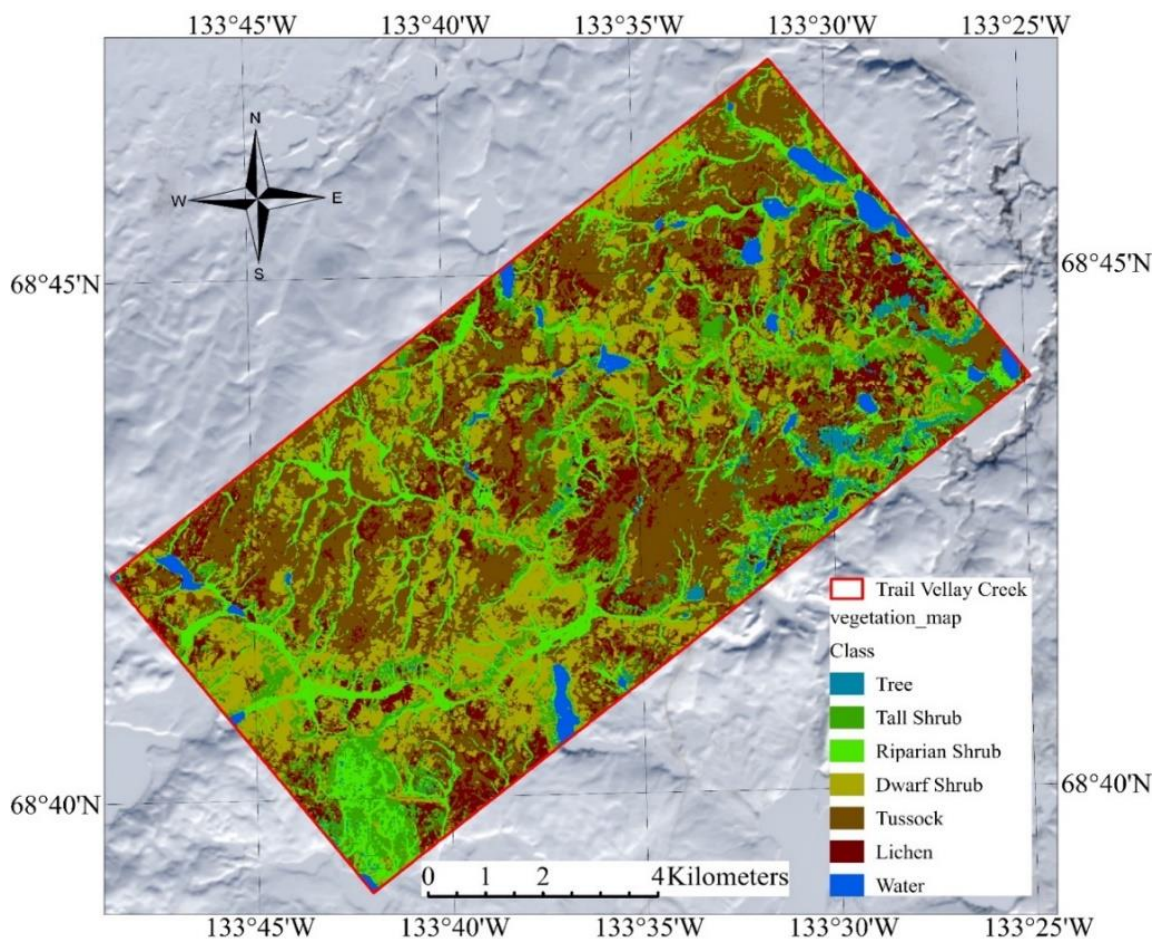
Figure 3. 4 Vegetation class map of the study area

3.3.4 TVC Digital terrain model and vegetation height map

An additional pivotal factor influencing backscatter intensity is the necessity for a high-resolution DTM to mitigate terrain-induced effects on the RSAT-2 SAR signal. To address this requirement, a snow-free ALS product specific to the TVC region was procured from Anders et al. (2018), recorded on September 13, 2016. Beyond the DEM, two supplementary products

derived from the ALS point cloud encompass data on the maximum vegetation height and the mean vegetation height. These vegetation height maps serve as references for the typical heights associated with various vegetation types. The specifications of these three products are elucidated in Figure 3.5. All three datasets have undergone processing to achieve a spatial resolution of 1m and have been georeferenced to the WGS 84/ UTM zone 8N coordinate system.
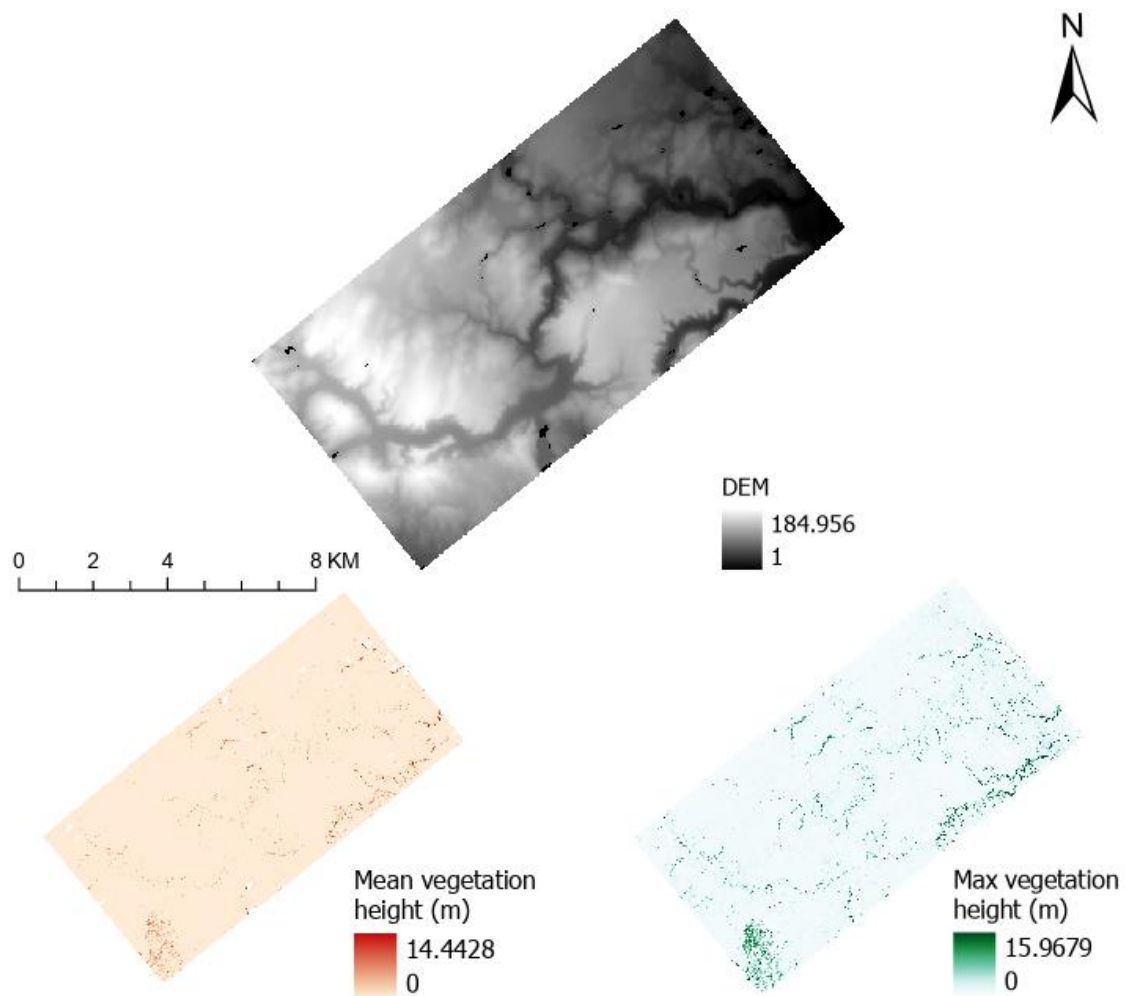
Figure 3. 5 Digital terrain model (top), maximum vegetation height (bottom left) and average vegetation height maps (bottom right) of study area.

3.4 Methodology

A flowchart summarizing the proposed methodology is shown in Figure. 3.6. It includes the following steps: data pre-processing, feature engineering and train-test split, sensitivity analysis, implementation of a snow depth retrieval algorithm from Lievens et al. (2019) and snow depth estimation from a DL approach.
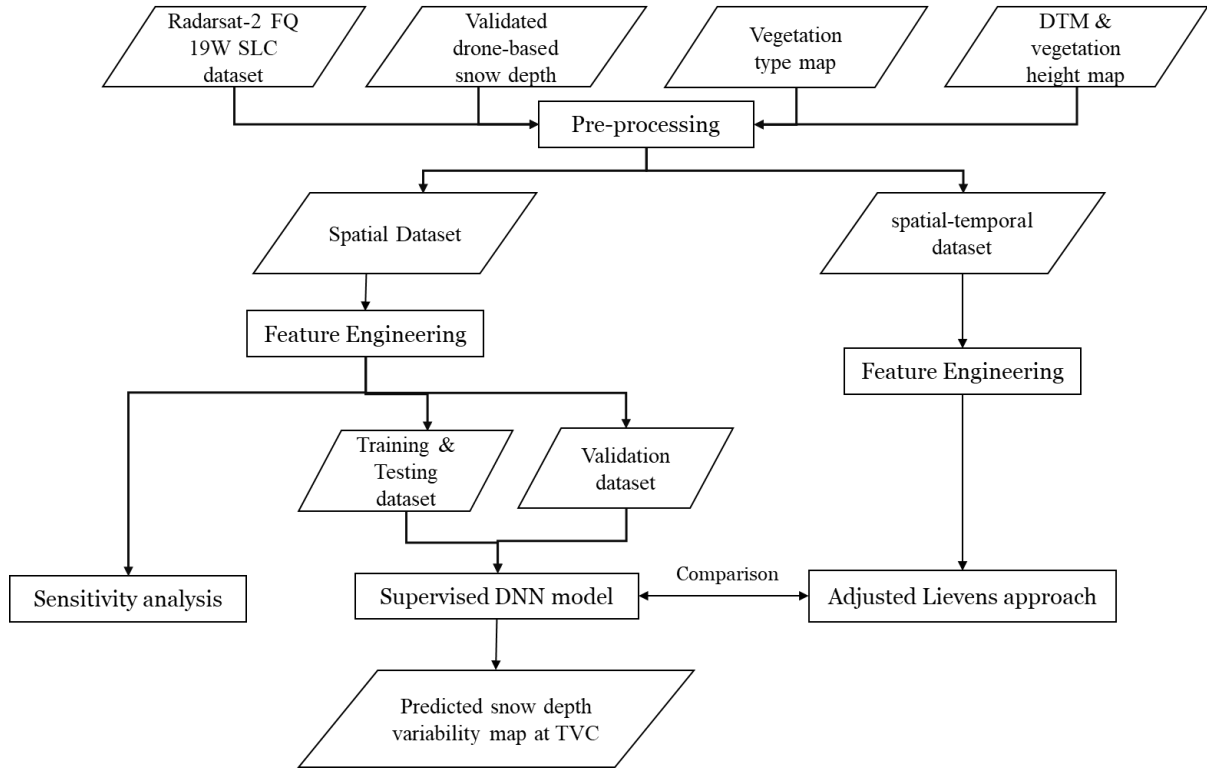
Figure 3. 6 Workflow diagram

3.4.1 Radarsat-2 vs Sentinel-1

Among C-band spaceborne SAR systems most utilized globally, Sentinel-1 from ESA and Radarsat-2 from CSA were most commonly used in recent research (Tsai et al., 2019). In TVC, the Sentinel-1 SLC product primarily relies on the Interferometric Wide (IW) beam mode. According to the data description of Sentinel-1 SAR (ESA, 2023), Table 3.2 conducts a foundational comparison between Sentinel-1 and Radarsat-2 under SLC data format. Compared to Sentinel-1, Radarsat-2 FQ19W SLC data offers a key edge with its ability to

perform fully polarimetric imaging at a higher spatial resolution. This allows for the generation of more accurate backscatter patterns under different polarizations, which is crucial for detailed analysis on snowpack. Furthermore, in the realm of SAR, Noise-Equivalent Sigma-Zero (NESZ) serves as a key metric reflecting the impact of system noise on image quality. Notably, Radarsat-2 boasts lower NESZ values than Sentinel-1, making it the preferred choice for detecting snow with weak backscatter signals.

Table 3. 2 Comparison between fundamental parameters of Radarsat-2 and Sentinel-1 in Single-look complex Product

	Radarsat-2	Sentinel-1
Beam Mode	Wide Fine Quad-Pol 19	Interferometric Wide
Polarization Options	Quad-Pol	Single (HH or VV) or
	(HH+HV+VV+VH)	Dual (HH+HV or VV+VH)
Spatial resolution	5 x 8 meter	5 x 20 meter
Incident angle	$37° – 40°$	$29.1° – 46.0°$
Swath coverage	$25 \times 50 \text{ km}^2$	250 km^2
Revisited day	24 days	12 days
Noise-Equivalent Sigma-Zero	-33 dB	-22 dB

3.4.2 Data Pre-processing

In this investigation, the pre-processing of RSAT-2 images was conducted through ESA Sentinel Application Platform. The pre-processing protocol for RSAT-2 Single-look Complex (SLC) data closely adhered to the methodology outlined by Lievens et al. (2019, 2022). This encompassed successive stages of radiometric calibration, terrain flattening to achieve backscatter in γ^0, multi-looking, speckle filtering, and Range-Doppler terrain correction. Terrain flattening serves to mitigate the impact of terrain, look angle, and local incident angle on backscatter intensity (Small, 2011). The application of terrain flattening, and terrain correction involved utilizing DTM data from Anders et al. (2016), as detailed in Section

3.3.4. The processed data underwent resampling to a 10m grid spacing to enhance radiometric resolution and reduce overall processing time. Additionally, the data were georeferenced to the WGS 84/ UTM zone 8N coordinate system to align with the reference data projection for snow depth. Moreover, corresponding local incident angle (LIA) and DEM datasets were generated with matching resolution and coordinates as the processed RSAT-2 imagery. Given the reliance on the CPR demonstrated by Lievens et al. (2019, 2022) for assessing C-band SAR sensitivity to snow depth, quad-polarization backscatter coefficients (γ_{VH}^0, γ_{HV}^0, γ_{VV}^0, γ_{HH}^0) were generated. These coefficients were subsequently utilized to compute the CPR value and were converted to the decibel (dB) scale. The specific equations governing the CPR calculations are expounded upon below:

$$CPR_{\frac{VH}{VV}} = \frac{\gamma_{VH}^0}{\gamma_{VV}^0} \quad \text{(dB)} \tag{3.2}$$

$$CPR_{\frac{VH}{HH}} = \frac{\gamma_{VH}^0}{\gamma_{HH}^0} \quad \text{(dB)} \tag{3.3}$$

$$CPR_{\frac{HV}{VV}} = \frac{\gamma_{HV}^0}{\gamma_{VV}^0} \quad \text{(dB)} \tag{3.4}$$

$$CPR_{\frac{HV}{HH}} = \frac{\gamma_{HV}^0}{\gamma_{HH}^0} \quad \text{(dB)} \tag{3.5}$$

For the drone-based snow depth reference data and vegetation height map, both will be aggregated to 10m spatial resolution with the mean method for fitting with the spatial resolution of processed RSAT-2 data. Finally, the processed RSAT-2 data were co-registered with vegetation class map, DTM, LIA, and vegetation height data to the dataset and clip to the corresponding AOIs extent of snow depth data.

To facilitate the subsequent numerical and deep learning methodologies, two distinct datasets were meticulously curated. The first dataset, referred to as the spatial-temporal dataset, encompasses 18 meticulously processed data instances. Meanwhile, the spatial dataset, integral to this study, incorporates three meticulously processed RSAT-2 data scenes. The selection of these scenes was conducted with utmost precision to closely align with the recorded dates of snow depth, as delineated in Table 3.3.

Table 3. 3 Summary of Radarsat-2 images that are close to the capture date of drone-based snow depth.

Drone-based snow depth data	Closed Radarsat-2 Product	Radarsat-2 Acquisition Dates
AOI 1 2018-04-22	RS2_OK96228_PK845567_DK776989_FQ19W _20180408_022222_HH_VV_HV_VH_SLC	2018-04-08
AOI 2 2018-03-12	RS2_OK95250_PK837907_DK768984_FQ19W _20180315_022223_HH_VV_HV_VH_SLC	2018-03-15
AOI 3 2018-03-13	RS2_OK95250_PK837907_DK768984_FQ19W _20180315_022223_HH_VV_HV_VH_SLC	2018-03-15
AOI 4 2018-03-13	RS2_OK95250_PK837907_DK768984_FQ19W _20180315_022223_HH_VV_HV_VH_SLC	2018-03-15
AOI 7 2018-03-16	RS2_OK95250_PK837907_DK768984_FQ19W _20180315_022223_HH_VV_HV_VH_SLC	2018-03-15
AOI 8 2018-03-16	RS2_OK95250_PK837907_DK768984_FQ19W _20180315_022223_HH_VV_HV_VH_SLC	2018-03-15
AOI 9 2018-03-20	RS2_OK95250_PK837907_DK768984_FQ19W _20180315_022223_HH_VV_HV_VH_SLC	2018-03-15
AOI 1 2019-04-10	RS2_OK107832_PK939911_DK876160_FQ19W _20190403_022201_HH_VV_HV_VH_SLC	2019-04-10
AOI 2 2019-04-10	RS2_OK107832_PK939911_DK876160_FQ19W _20190403_022201_HH_VV_HV_VH_SLC	2019-04-10

3.4.3 Feature Engineering and Data Cleaning

In the development of retrieval algorithms and the implementation of DL approach, the influence of system noise, leading to outliers, errors, and uncertainty, necessitates meticulous attention. To mitigate these effects, a prerequisite for prior knowledge incorporation was recognized to eliminate potential noise and uncertainty within the dataset. Notably, the RSAT-2 FQ19W Single-look Complex (SLC) data established a -33dB NESZ threshold, effectively constraining noise in the cross-polarized backscatter response. Samples with a local incidence angle exceeding 60 degrees were systematically excluded to diminish radar shadowing effects.

Concurrently, in drone-based snow depth products, inherent errors, including negatives and inaccuracies attributed to the DEM, prompted the imposition of constraints. The snow depth values were confined to the range of 0.01 to 4 meter, effectively disregarding areas with negative values and those deemed snow-free. Additionally, manual masking was employed to eliminate tree heights from all snow depth products. Considering the documented attenuation

of snow backscatter by forest cover above the snowpack (Tsang et al., 2022; Macelloni et al., 2012), vegetation heights exceeding the snow depth were systematically excluded from both the maximum vegetation height map and the mean vegetation height map.

Furthermore, the study excluded considerations for snow on the lake ice interface, necessitating attention to samples located in the water class. For optimal effectiveness in deep learning approach applications, all "no data" values and error values within existing data pairs were systematically excluded. These comprehensive steps were consistently applied to both spatial and spatial-temporal datasets. The processed samples ensuing from these stringent measures served a multitude of purposes, including sensitivity analysis, plot generation, and implementation of snow depth estimation from numerical and deep learning approach.

3.4.4 Sensitivity analysis between SAR backscattering and Snow depth change

Lievens et al. (2019) undertook a temporal analysis, scrutinizing the behavior of Sentinel-1 backscatter during the winter season at a spatial resolution of 1 kilometer. Their observations revealed that co-polarization (co-pol) backscatter demonstrated relatively limited variation, predominantly influenced by ground surface characteristics rather than fluctuations in the thickness of the dry snowpack. In contrast, cross-polarization (cross-pol) backscatter measurements exhibited a gradual augmentation concomitant with the accumulation of dry snow. The researchers postulated that this elevation in backscatter was attributable to the augmented thickness of the snowpack, which elongates the path of radar signal, creating increased opportunities for scattering within the snowpack. Furthermore, they posited that, at a given snow depth, snow volume scattering played a principal role in total backscatter in cross-pol, surpassing the contribution of ground surface scattering. Consequently, the CPR demonstrated a heightened correlation with snow depth, owing to its partial mitigation of the influences stemming from the ground surface, vegetation, and snow conditions. It is imperative to highlight that the discerned reliability of CPR in capturing sensitivity to snow depth pertains predominantly to snowpacks surpassing a depth threshold of 0.5 meters.

Therefore, for evaluating the CPR method sensitivity to deep tundra snow using RSAT-2 SAR observations for different snow depth variability, the following analysis was presented based on the above description of CPR from Lievens et al. (2019):

1. Analyze the CPR, cross-pol, and co-pol backscatter pattern on each 0.5m bin of snow depth.
2. Test the CPR, cross-pol, and co-pol backscatter correlation on a series of thresholds of 0.5, 1, 1.5, and 2.5 m snow depth.
3. Analyze the sensitivity of CPR, cross-pol, and co-pol backscatter to snow depth under different vegetation types and landscapes.
4. Analyze the temporal change of CPR value on the various snowpack location.

3.4.5 Implementation of Lievens snow depth retrieval algorithm in TVC

Referring to the research of Lievens et al. (2019), the proposed snow depth retrieval algorithm is an empirical method that combines the change detection snow index with the CPR and the empirical adjustment from forest cover fraction (FCF) and in-situ SD measurements to estimate snow depth in mountainous areas of the northern hemisphere at 1000 m spatial resolution. The equation of change detection snow index (SI) is calculated as:

$$SI(i,t) = \begin{cases} \max\left(0, [SI(i, t-1) + CPR_{\frac{VH}{VV}}(i,t) - CPR_{\frac{VH}{VV}}(i, t-1)]\right) & if\ SC\ (i,t) = 1 \\ 0 & if\ SC\ (i,t) = 0 \end{cases} \quad (3.6)$$

where i refers to each location (or pixel) and t refers to the time step of each location. This empirical snow index is the main part that represents the sensitivity of the CPR to snow accumulation (snow depth increase). With the calculated snow index at each time step, the SD is shown as:

$$SD\ (i.t)\ = \left(\frac{a}{1-b\ FC(i)}\right) SI(i,t) \qquad (meter) \qquad (3.7)$$

where the empirical index a (m / dB) and b is constant in location (i) and time step (t), and FC(i) is the forest cover fraction.

In Equation (3.6), the empirical snow index stands as the primary component of the retrieval algorithm, serving to deduce the spatial-temporal correlation between the CPR and snow depth. Equation (3.7), conversely, plays a supplementary role, strategically employed to mitigate the impact of forest cover on snow backscatter and address the inherent errors in measured data. From the perspective of the change detection algorithm, the SI value is computed through the aggregation of Sentinel-1 observations at a spatial resolution of 1 kilometer. This aggregation not only markedly diminishes speckle noise intrinsic to SAR data but also alleviates geometric distortions prevalent in regions characterized by complex topography.

Within TVC study area, statistical analyses of SD distribution reveal dominance by shallow snow depths ranging from 0.5 to 1 meter. The aggregation of SAR observations contributes significantly to smoothing the features of deep snowpacks within the 1 km² area. Considering the forest cover fraction in Equation (3.7), this value is utilized to factor in the influence of forest cover on the calculated SI. Notably, apparent evergreen forest or vegetation existing above the snowpack has been systematically excluded in Section 3.4.3. Additionally, it is important to underscore that the forest cover fraction is not applicable at high spatial resolutions.

Given the unique circumstances in implementing the Lievens algorithm in TVC, a nuanced adjustment is introduced to ensure the algorithm's applicability in scenarios characterized by deeper snowpacks:

- The snow index will be calculated at the 10 m spatial resolution for keeping more features of deep snowpack in TVC.
- Due to the lack of spatio-temporal snow depth, the adjusted Lievens approach were only validated with time step that has drone-based snow depth.
- Since there are lack of FCF value at high spatial resolution, the equation (3.7) will be changed to:

$$SD\,(i.t) = a * SI(i,t) + b \tag{3.8}$$

where coefficients a and b are obtained by minimizing the mean average error between the calculated SI and snow depth reference at 10 m spatial resolution.

3.4.6 Snow Depth Estimation by Deep Neural Network

In the context of this study, the estimation of snow depth from SAR data is fundamentally approached as a regression problem. The Deep Neural Network (DNN) is systematically trained to address this problem, utilizing a paired spatial dataset generated in Section 3.4.2, structured according to the general formula outlined below:

$$y = f(X, p) \tag{3.9}$$

where Y represents the drone-based snow depth data, serving as the predictand variable, while X denotes the corresponding processed RSAT-2 data, encompassing SAR backscatter information, CPR, terrain, and vegetation class information, collectively constituting the predictors. The detailed variables are listed in Table 3.4. The parameter p signifies the parameters intrinsic to the neural network. The implementation of the DL method is primarily executed on the spatial dataset established in Section 3.4.2. The spatial dataset will be normalized to the range (0, 1) using the min-max technique. This normalized data will then be randomly partitioned into training (25%), testing (25%), and validation (50%) subsets to facilitate effective model training and evaluation.

Table 3. 4 Summary of predicted variables in DL approach

Input predicted variables	
SAR Gamma backscatter	VH-pol, VV-pol, HV-pol, HH-pol
Calculated CPR value	$CPR_{VH/VV}$, $CPR_{VH/HH}$, $CPR_{HV/VV}$, $CPR_{HV/HH}$
Terrain information	DEM, local incident angle
Vegetation information	Vegetation class, mean vegetation height, max vegetation height

Building on the established correlations between snow depth and SAR data elements observed by Lievens et al. (2019), understanding the relative importance of terrain and vegetation parameters in DNN models predicting snow depth from SAR data remains

enigmatic. To illuminate this hidden influence, there are two distinct parameter configurations will be tested:

1. SAR Data Alone: This configuration excludes terrain and vegetation information, functioning as a baseline. It allows to assess the predictive power of SAR data by itself, independent of other influencing factors.

2. SAR Data with Terrain and Vegetation: This configuration incorporates the full spectrum of available information, encompassing SAR alongside terrain and vegetation parameters. This inclusion aims to unveil the potential synergistic effects or counter-contributions of these additional parameters, revealing their impact on the DNN model's accuracy in predicting snow depth.

In this study, the Multi-Layer Perceptron (MLP) neural network was selected for snow depth estimation, which has been widely used in regression tasks, The MLP encompasses one or more hidden layers, which are fully interconnected. Also, each comprises a specific number of neurons and non-linear activation functions. This layered structure makes MLP able to handle non-linear data and learn complex patterns without explicitly mapping the data to another high-dimensional space. Snow depth and its relationship with environmental factors like SAR data, terrain, and vegetation often involve complex, non-linear connections. MLPs excel in capturing these intricate relationships.

Compared to other machine learning techniques like Support Vector Machines (SVMs), MLP offer several key advantages for estimating snow depth. Snow depth and its relationship with SAR data and environmental factors often dance a non-linear tango. MLPs, with their layered structure and non-linear activation functions, are adept at capturing these intricate patterns. Unlike SVMs which favor linear boundaries and clear relation, MLPs can flexibly model diverse patterns without needing explicit feature extraction. Also, MLP can seamlessly handle a large number of input variables, allowing you to incorporate all potentially relevant information like SAR data, terrain and vegetation cover, for a more comprehensive analysis. SVMs, while powerful, can become computationally sluggish with high-dimensional data. Since SAR data always inherent noise and errors, MLP offer greater tolerance for noise

and outliers compared to SVMs. They can adapt to noisy or incomplete data points without sacrificing accuracy as much as SVMs might. Furthermore, MLP training can be significantly accelerated using GPUs, while SVMs remain confined to the slower lanes of CPUs. When training the model with a large dataset (about 300,000 data pairs) on a Windows 10 desktop with an Intel 12700 CPU and NVIDIA RTX3060Ti GPU, an MLP model took only 1 hour to be trained by the efficient GPU acceleration. In contrast, the SVM took over 12 hours due to its less GPU-friendly nature. This dramatic speed difference is particularly critical for personal desktops due to limited processing power and the desire for fast results. The superior performance of MLP on GPUs likely stems from its efficient utilization of parallel processing and memory bandwidth compared to SVM. As demonstrated by Santi et al. (2019), MLP neural networks have already showcased their effectiveness in estimating snow depth from X-band and Ku-band SAR data within the TVC.

The training procedure relies on the backpropagation (BP) learning rule, aiming to minimize the loss function that quantifies the discrepancy between the training output and the target value. This minimization is achieved by iteratively adjusting the weights and biases to either suppress or enhance the connections. To navigate towards the global minima of the loss function, an optimizer is imperative to execute gradient descent. The general architecture of an MLP is illustrated in Figure 3.7.
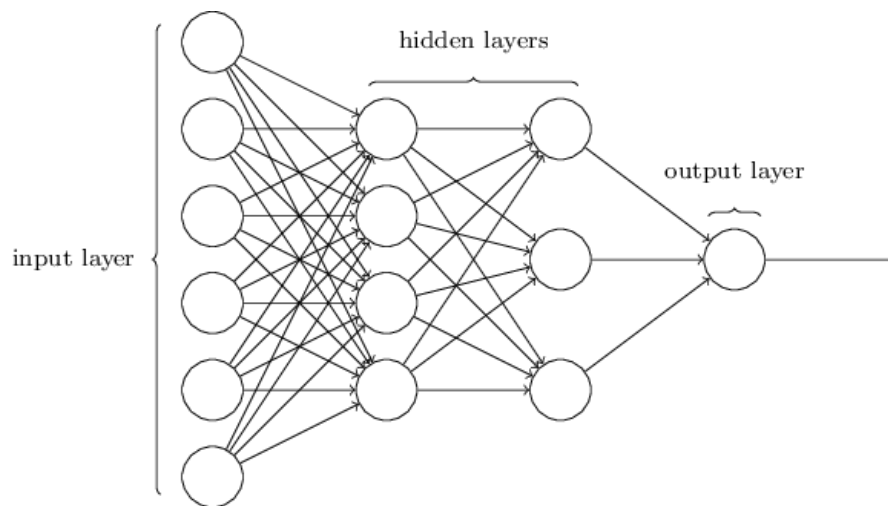
Figure 3. 7 Simple structure of MLP NN

The DNN is characterized by an increased number of hidden layers and neurons, signifying a deeper and more complex neural architecture. In pursuit of depth, additional hidden layers, featuring identical neurons and activation functions, are incorporated into the original MLP. This expansion aims to enhance the network's capacity for abstraction and feature extraction.

To optimize the predictive performance for snow depth, a meticulous process of hyperparameter tuning is implemented. The model parameters subject to tuning encompass the number of hidden layers, the quantity of neurons within each layer, the choice of activation function, the selection of loss function, and the optimizer. The determination of these model parameters hinges on the iterative reduction of loss in the training dataset and the concurrent enhancement of predicted accuracy metrics, such as correlation coefficient and RMSE, on the testing dataset.

To preemptively address the issue of overfitting, the initial number of epochs (iterations) is set to 200. In the absence of significant improvement, signified by no reduction in loss over 50 consecutive epochs during training, the process halts. Conversely, if the training process exhibits a continuous reduction in loss, the epochs persistently increase. This approach ensures a balance between model complexity and generalization performance.

3.4.7 Evaluation Metrics

When evaluating the estimation performance of SD estimation from numerical and DL approach, the conventional accuracy metrics will be used: R (Pearson's correlation coefficient), RMSE (root mean square error), MAE (mean average error). The equations are shown as:

$$R = \frac{\sum_{i=1}^{n} (x_i - \bar{x})(y_i - \bar{y})}{\sqrt{\sum_{i=1}^{n} (x_i - \bar{x})^2 \sum_{i=1}^{n} (y_i - \bar{y})^2}} \qquad (3.10)$$

$$RMSE = \sqrt{\frac{1}{n} \sum_{i=1}^{n} (x_i - y_i)^2} \qquad (3.11)$$

$$MAE = \frac{1}{n} \sum_{i=1}^{n} |x_i - y_i| \qquad (3.12)$$

where $\bar{x}$ is the mean value of all predicted values x_i, $\bar{y}$ is the mean value of all target values y_i, and n denotes the amount of data used.

3.5 Results

3.5.1 Sensitivity analysis of Radarsat-2 backscattering to snow depth change

In this section, an analysis is conducted on the spatial dataset generated in Section 3.4.2, comprising approximately 300,000 samples across diverse locations and temporal instances. Figure 3.8 illustrates the variations in Gamma backscatter for each polarization state within distinct snow depth bins. For co-polar backscatter (HH, VV), the primary backscatter generally fluctuates between -13 to -17 dB across different snow depth bins, displaying no discernible trend indicative of co-pol sensitivity to varying snow depths. Notably, for shallow snow depths (0 to 2 m), co-pol backscatter exhibits significant variability within -10 to -20 dB. However, this variability suggests that shallow snow depth alone is not a definitive indicator affecting backscatter intensity. The results indicate that co-pol backscatter is generally insensitive to changes in shallow snow depth within tundra snow environments, aligning with the findings of Lievens et al. (2019). Beyond 2 m snow depth, a gradual decline (~ 0.5 dB) in primary co-pol backscatters is observed with increasing snow depth, hinting at potential sensitivity to deeper snow layers. Comparing HH and VV backscatter with deep snow depth, VV polarization appears to exhibit a more pronounced sensitivity than HH polarization.

Contrasting co-pol, cross-pol backscatter (VH, HV) demonstrates a more noticeable increasing trend with snow depth. In the 0 to 1 m snow depth range, cross-pol backscatter fluctuates between -33 and -21 dB, with the primary backscatter features concentrated between -28 and -26 dB. The results reveal that cross-pol backscatter is not sensitive to shallow snow depth, even in tundra environments. A positive trend is observed in cross-pol, with an approximate 0.5 dB increase corresponding to snow depth bin increments. This suggests that the 1 m snow depth acts as a threshold for the initiation of cross-pol sensitivity to snow depth changes. However, the considerable variation implies a limited sensitivity. Consistent with the observations of Lievens et al. (2019), cross-pol sensitivity becomes evident only with snow

depths exceeding 0.5 m. Beyond 2 m snow depth, the sensitivity of cross-pol increases with a smaller variation range, reaching higher sensitivity as snow depth exceeds 3 m. This contrast sharply with backscattering characteristics observed at snow depths below 1 m. Comparing HV and VH polarizations, the plots indicate that VH polarization may exhibit superior performance in capturing snow depth changes compared to HH polarization.
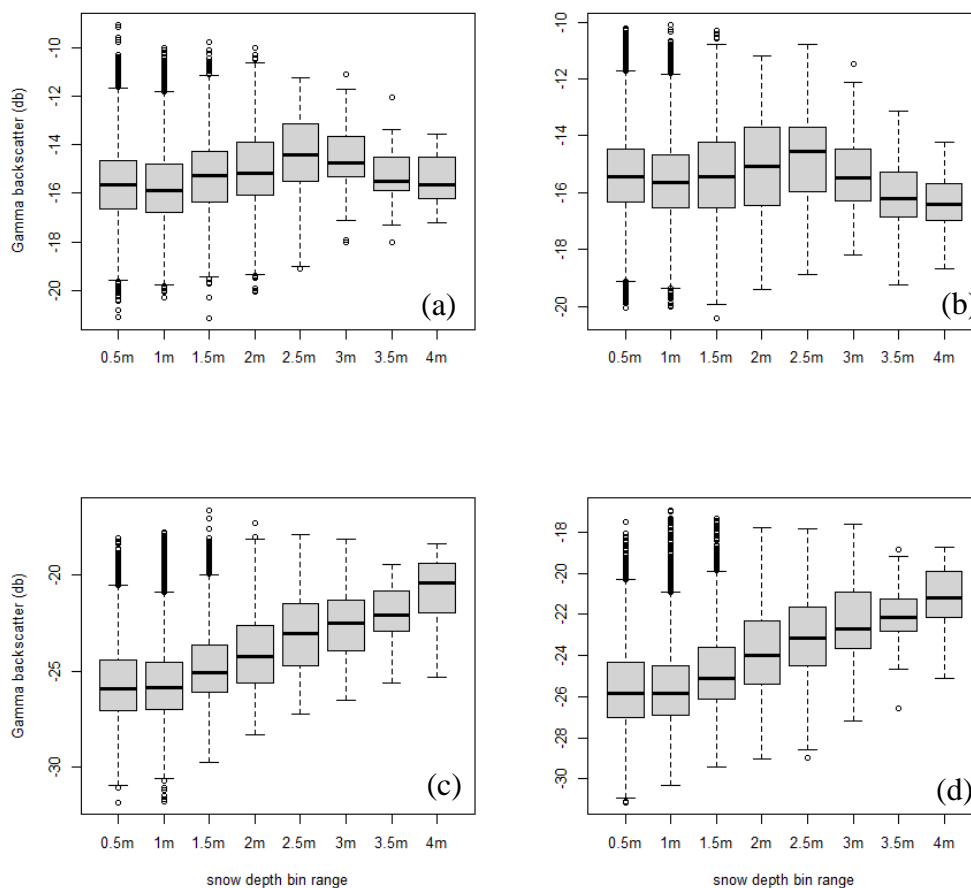
Figure 3. 8 The RSAT-2 backscatter variations on snow depth of all AOIs for different polarization states: (a) HH-pol Gamma backscatter, (b) HV-pol Gamma backscatter, (c) VV-pol Gamma backscatter and (d) VH-pol Gamma backscatter.

In Figure 3.9, a comparison is presented between four CPRs concerning changes in snow depth. As the CPR value is derived from cross-pol and co-pol backscatter, the trends of CPR values closely align with cross-pol rather than co-pol, attributable to the more pronounced

variation in cross-pol backscatter. In the snow depth range of 0 to 1 m, the distribution of CPR values mirrors the behavior of cross-pol, remaining constant at the lowest level. Moreover, CPR begins to exhibit sensitivity (approximate 0.5 dB increase) with snow depths exceeding 1 m. Notably, when snow depth surpasses 2 m, CPR becomes more sensitive to changes in snow depth, possibly as co-pol starts to manifest sensitivity to deeper snow layers. Consequently, the CPR method demonstrates an enhanced sensitivity to changes in snow depth compared to individual cross-pol and co-pol measurements.
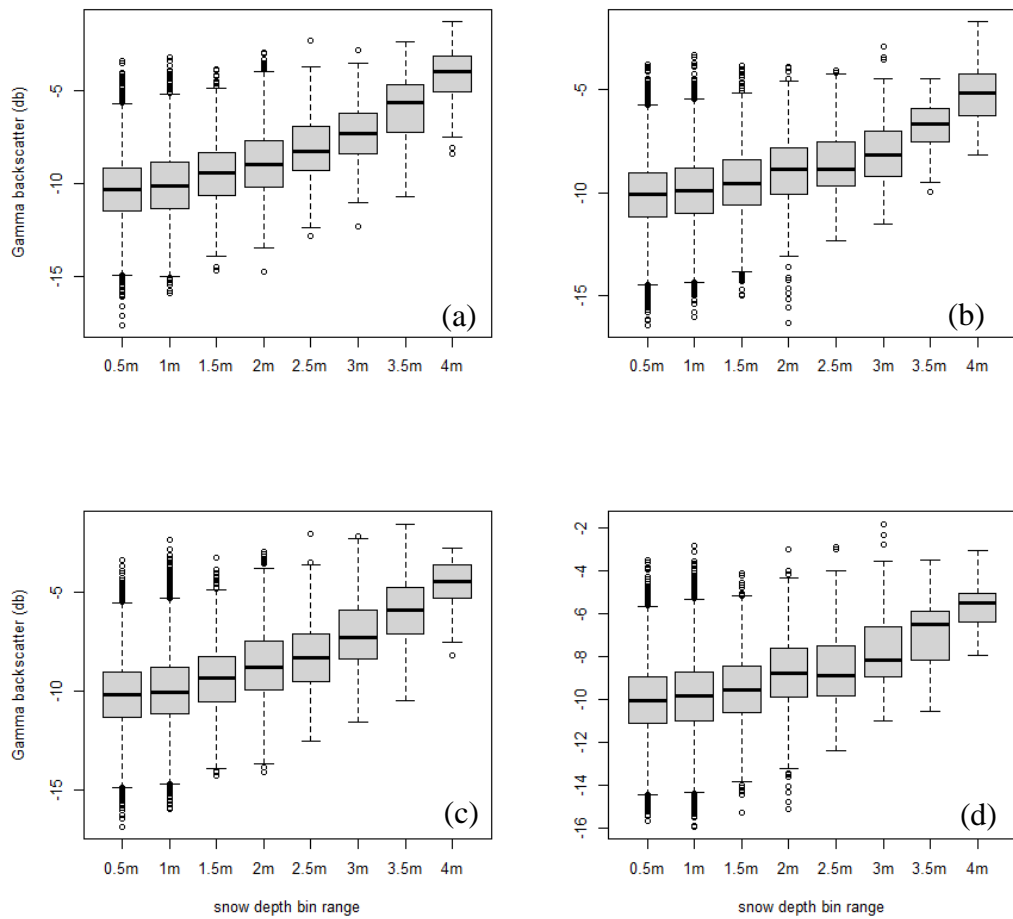
Figure 3. 9 Comparison of the RSAT-2 CPR variations on snow depth of all AOIs for different CPR combinations: (a) **CPR$_{VH/VV}$** (b) **CPR$_{VH/HH}$** (c) **CPR$_{HV/VV}$** and (d) **CPR$_{HV/HH}$**

Table 3.5 provides a comparative analysis of cross-pol, co-pol, and CPR across various snow depth ranges. Across the entire spectrum of snow depth, both cross-pol and co-pol

backscatter exhibit a generally low positive correlation with snow depth, consequently yielding a CPR value with limited correlation to snow depth. The introduction of the cross-pol to co-pol ratio, however, tends to amplify the positive correlation with snow depth, surpassing that of individual polarizations. As samples with shallow snow depth are progressively excluded, the correlation of cross-pol and CPR values with snow depth steadily rises. Notably, co-pol backscatter within the domain of deep snow depth registers an increasingly negative correlation with snow depth. The correlation between cross-pol and snow depth tends to stabilize, particularly in regions where snow depth exceeds 2m. Conversely, the negative correlation between co-pol and snow depth intensifies, contributing to a more robust positive correlation between CPR and snow depth. Consequently, a potential threshold for CPR sensitivity to tundra snow depth could be set at 2m, as the highest correlation (0.52) is attained beyond this threshold. In comparing the correlation of four CPR values across different snow depth ranges, CPR derived from VH and VV consistently achieves the highest correlation in each snow depth range, suggesting a potentially stronger sensitivity to snow depth than other CPRs. Nevertheless, the correlation between CPR and deeper snowpack remains inferior to that demonstrated by Lievens in mountainous regions.

Table 3. 5 Pearson's correlation coefficient between each polarized gamma backscatter, CPR, and different snow depth ranges

	Full snow depth	Over 0.5 m snow depth	Over 1 m snow depth	Over 1.5 m snow depth	Over 2 m snow depth	Over 2.5 m snow depth
	$(0-4\text{ m})$	$(0.5-4\text{ m})$	$(1-4\text{ m})$	$(1.5-4\text{ m})$	$(2-4\text{ m})$	$(2.5-4\text{ m})$
γ_{HH}^0	-0.01	0.09	0.02	0.03	-0.25	-0.28
γ_{HV}^0	0.14	0.27	0.25	0.28	0.29	0.21
γ_{VH}^0	0.14	0.28	0.28	0.31	0.28	0.28
γ_{VV}^0	-0.06	0.01	-0.05	-0.13	-0.31	-0.27
$CPR_{\frac{VH}{VV}}$	0.22	0.31	0.37	0.46	0.52	0.47
$CPR_{\frac{VH}{HH}}$	0.18	0.24	0.32	0.40	0.50	0.51
$CPR_{\frac{HV}{VV}}$	0.21	0.30	0.38	0.44	0.49	0.43
$CPR_{\frac{HV}{HH}}$	0.18	0.23	0.32	0.38	0.47	0.47

While Lievens et al. (2019) suggest that CPR could mitigate the influence of vegetation on snow depth, the diverse vegetation cover in TVC is likely to impact SAR backscatter still significantly. The significant influence of different vegetation classes on SAR backscatter in TVC warrants further exploration. Quantifying this impact holds the potential to significantly improve the accuracy of snow depth estimates in arctic tundra regions. Figure 3.10 presents the sensitivity analysis of $CPR_{VH/VV}$, VH and VV on different snow depths under different vegetation types. Though all vegetation types, the more than 3 m snow depth only exists in the shrub area, primarily tall and riparian shrubs, and the shallow snow depth (less than 2 m) is concentrated in dwarf, tussock, and lichen vegetation types. The tall shrub and riparian shrub areas likely accumulated deep snow at the end of winter. In comparing the VH (cross-pol) sensitivity within different vegetation types, the backscatter variations are less for snow depth increase in dwarf shrubs, tussock and lichen, and the apparent variation only exists in the tree, tall shrub, and riparian shrubs area. Also, the VH backscatter shows a more noticeable increase in snow depth under the riparian shrub area than others. For the VV (co-pol) backscatter, the variation generally remains constant in the tree dwarf shrub, and an overt decrease trend could only exist in the riparian shrub, tall shrub, and tussock with over 2 m snow depth. Under the different vegetation types, the CPR variation not only depends on the cross-pol behavior with snow depth change, but the sensitivity of co-pol to snow depth can also make CPR somewhat sensitive to snow depth. In the tussock area, the decrease in cross-pol and unchanged in cross-pol backscatter will make the CPR sensitive to snow depth. In the deep snow depth, as an increase in cross-pol and co-pol decreases, the CPR will achieve a higher increase with snow depth, enhancing the sensitivity of CPR to snow depth. Therefore, the CPR method will be more valid within the tall shrubs and riparian shrubs and may not work in lichen-covered areas.
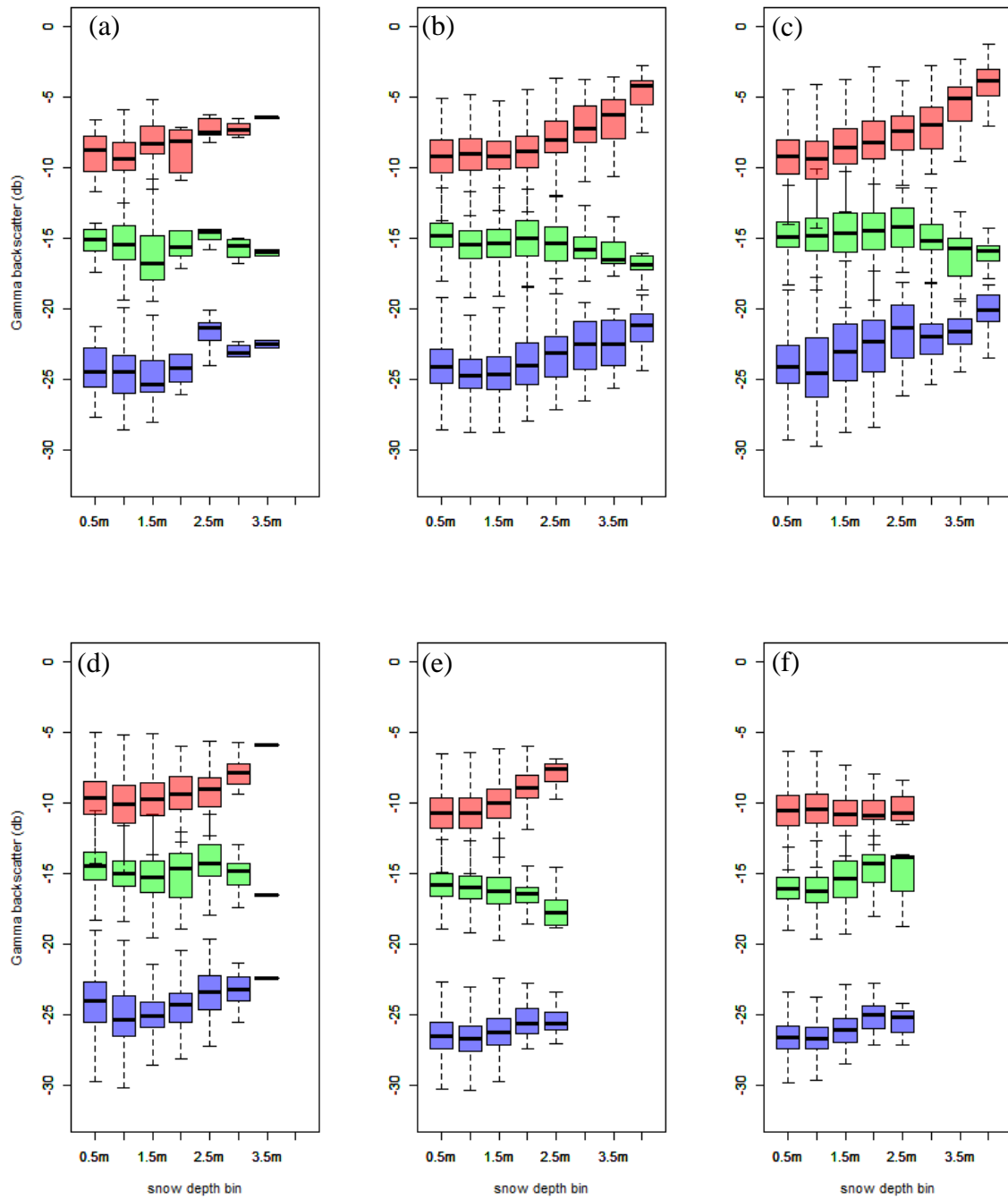
Figure 3. 10 The VH-pol backscatter (blue), VV-pol backscatter (green), corresponding CPR (red) variations on snow depth of all AOIs under following vegetation class: (a) tree, (b) tall shrub, (c) riparian shrub, (d) dwarf shrub, (e) tussock and (f) lichen.

Figure 3.11 depicts the temporal evolution of VH, VV, and CPR backscatter across various snow depth ranges over the entire winter period in 2018 and 2019, with each time step corresponding to RSAT-2 image acquisition dates. A comparison of temporal SAR data changes in different snow depth ranges reveals significant backscatter variations only in the deep snow depth (3 - 4 meters) locations in 2018 or 2019; other snow depth ranges exhibit an inconspicuous trend on the temporal scale, suggesting that temporal backscatter variations are primarily observable in deeper snow locations. The spatial dataset analysis indicates that SAR backscatter variations at each time step reflect changes in snow depth without requiring spatial-temporal snow depth references. The drone-based snow depth data, captured at the end of winter, implies that locations with 3 - 4 meters of snow depth will maintain deep snow. Consequently, locations with deeper snowpacks are assumed to accumulate snow (increasing in thickness) throughout the winter, while areas with shallow snow depth at the end of winter are unlikely to accumulate deeper snow. Following this assumption, co-pol backscatter generally exhibits a decreasing trend at deeper snowpack locations at each time step, likely due to increased snowpack thickness during the winter. Cross-pol backscatter undergoes rapid changes during winter in response to snow depth variations. From September to December, the significant decrease in cross-pol may result from snow melt and wind exposure. Subsequently, the increasing trend of cross-pol after January may signify snow accumulation. In the plot, the temporal trend of CPR values primarily reflects changes in cross-pol; the decreasing co-pol enhances the sensitivity of CPR to snow depth changes. Additionally, the highest CPR features captured in March suggest the likely formation of a deeper snowpack. In contrast, shallow snowpack areas exhibit distinct backscatter behaviors compared to deep snowpack locations. With cross-pol decreasing and co-pol remaining constant throughout the winter, the CPR value also remains at a lower level, confirming the limited sensitivity of C-band SAR to shallow snowpacks.
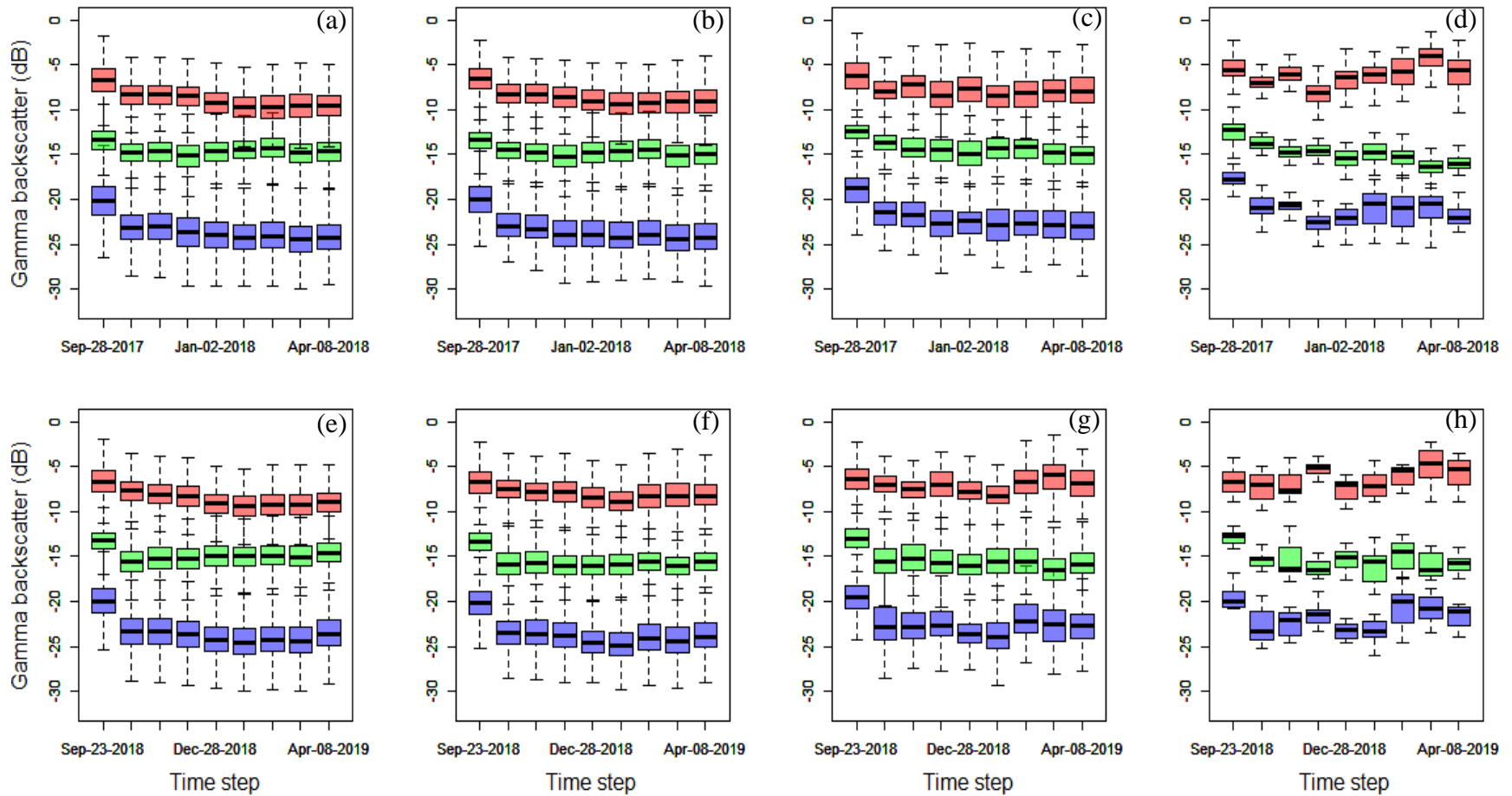
Figure 3. 11 Temporal variation of cross-pol (blue), co-pol (green) and corresponding CPR value (red) on different snow depth ranges through 2018 and 2019 AOIs. (a) 0 to 1 m snow depth location in 2018 AOIs, (b) 1 to 2 m snow depth location in 2018 AOIs, (c) 2 to 3 m snow depth location in 2018 AOIs, (d) 3 to 4 m snow depth location in 2018 AOIs, (e) 0 to 1 m snow depth location in 2019 AOIs, (f) 1 to 2 m snow depth location in 2019 AOIs, (g) 2 to 3 m snow depth location in 2019 AOIs and (h) 3 to 4 m snow depth location in 2019 AOIs.

Based on the aforementioned analysis, the findings from the sensitivity analysis can be summarized as follows:

1. In the context of TVC, characterized by tundra snow conditions, the response of RSAT-2 observations generally aligns with the Sentinel-1 observations made by Lievens in mountainous regions regarding C-band SAR sensitivity. However, the linear relationship between the CPR value derived from RSAT-2 and deep snow is present but may not exhibit a robust correlation. The CPR exhibits a stronger correlation with snow thickness compared to individual cross-pol and co-pol measurements in most scenarios. This implies that CPR is a more effective indicator of snow depth. Exceeds 2.5 meter snow depth, the co-pol also shows minor sensitivity to depth increase.

2. Lievens identified that C-band SAR sensitivity becomes apparent when snow depth exceeds 0.5 meters in mountainous regions. In the tundra snow environment, our analysis suggests that the threshold for sensitivity may be higher, around 2.5 meters of snow depth. Notably, RSAT-2 data does not demonstrate significant sensitivity to shallow to moderate snow depths, particularly when considering its high spatial resolution.

3. The sensitivity of the CPR method varies depending on the underlying vegetations. Which are the highest in areas with tall vegetation, such as tall shrubs and riparian shrubs. There is a threshold of approximately -25 dB in CPR value that distinguishes tall vegetation areas from low vegetation areas.

4. From a spatiotemporal perspective, C-band signal sensitivity to snow accumulation appears to be effective primarily in areas with a higher likelihood of accumulating deeper snowpack, such as drift areas or gullies. This suggests that the effectiveness of the C-band SAR signal in capturing snow accumulation varies spatially and is contingent on local topographical features.

3.5.2 Result of adjusted Lievens snow depth retrieval algorithm in TVC

This section leverages the spatial-temporal dataset from Section 3.4.2 to execute the adapted snow depth retrieval algorithm. The drone-based snow depth reference data, sourced

51

from various years and locations, necessitates the computation of the change detection-based SI and linear regression-based adjusted indexes (a and b) separately. As established in the preceding analysis (Section 3.5.1), RSAT-2 backscatter exhibits negligible sensitivity to shallow snow. Consequently, the efficacy of snow depth retrieval is constrained to locations capable of accumulating substantial snowpack. Accordingly, areas with potential shallow snow depth (such as tussock, lichen, and dwarf shrub regions) are excluded before the snow index calculation for the years 2018 and 2019.

The snow index calculation entails the determination of the difference between two observed Co-Polarization Ratios (CPRs) to depict snow depth changes at each time step. A positive SI signifies an increase in snow depth, influencing subsequent SI calculations, while a negative SI denotes snowmelt or disappearance. Instances where SI values equal 0 at a given time step prompt their removal for accurate snow depth estimation (Equation 3.7). Also, Within the entire range of snow depth, the optimized a and b coefficients are 0.5 and 0, respectively. Beyond 2.5 meters, these coefficients differ, with a becoming 0.12 and b increasing to 2.7.

Due to the drone-based snow depth data collected in different locations and month (March and April 2018 and April 2019); Figure 3.12 compares the result of adjusted Lievens approach estimates with drone-based snow depth references separately. In 2018, Figure 3.12a and Figure 3.12b, where no exclusion of shallow snow depth data was applied, the estimated results revealed a low correlation (0.12) with elevated RMSE and MAE values of 0.8 m and 0.62 m, respectively. This underscores the low capacity of the adjusted Lievens algorithm to accurately estimate snow depth across the complete snow depth range of TVC, suggesting the absence of a linear relationship between snow depth and SI. Upon exclusion of shallow snow depth samples in the 2018 (0 – 2.5 m), a more pronounced linear relationship between deep snow depth and SI emerges, resulting in an improved correlation (0.51) and reduced RMSE (0.38 m) and MAE (0.31 m).

The estimated results in 2019, encompassing the full snow depth range, yields a lower correlation (0.02), yet exhibits lower RMSE (0.93 m) and MAE (0.73 m) compared to 2018. In snow depths exceeding 2.5m, the correlation (0.27) remains insufficient to establish a robust

linear relationship between snow index and snow depth. However, the lower RMSE (0.35 m) and MAE (0.3 m) relative to 2018 can be attributed to snow thicknesses falling below the threshold values for the applicability of approach.

Considering the performance of the adapted algorithm in estimating deeper snow depth, it appears reasonable and effective within a tundra snow environment at high spatial resolution. In comparison to the Lievens approach (2019), the MAE of the Lievens method in the mountain area is 0.31m, akin to the MAE (0.31 m) of the adjusted Lieven approach at TVC. However, Lievens et al. (2019) reports a superior correlation coefficient (0.65) compared to the adjusted approach. Given that the adjusted approach achieves its highest correlation (0.51) solely in the context of deep snow depth, certain limitations persist in comparison to the Lievens method.
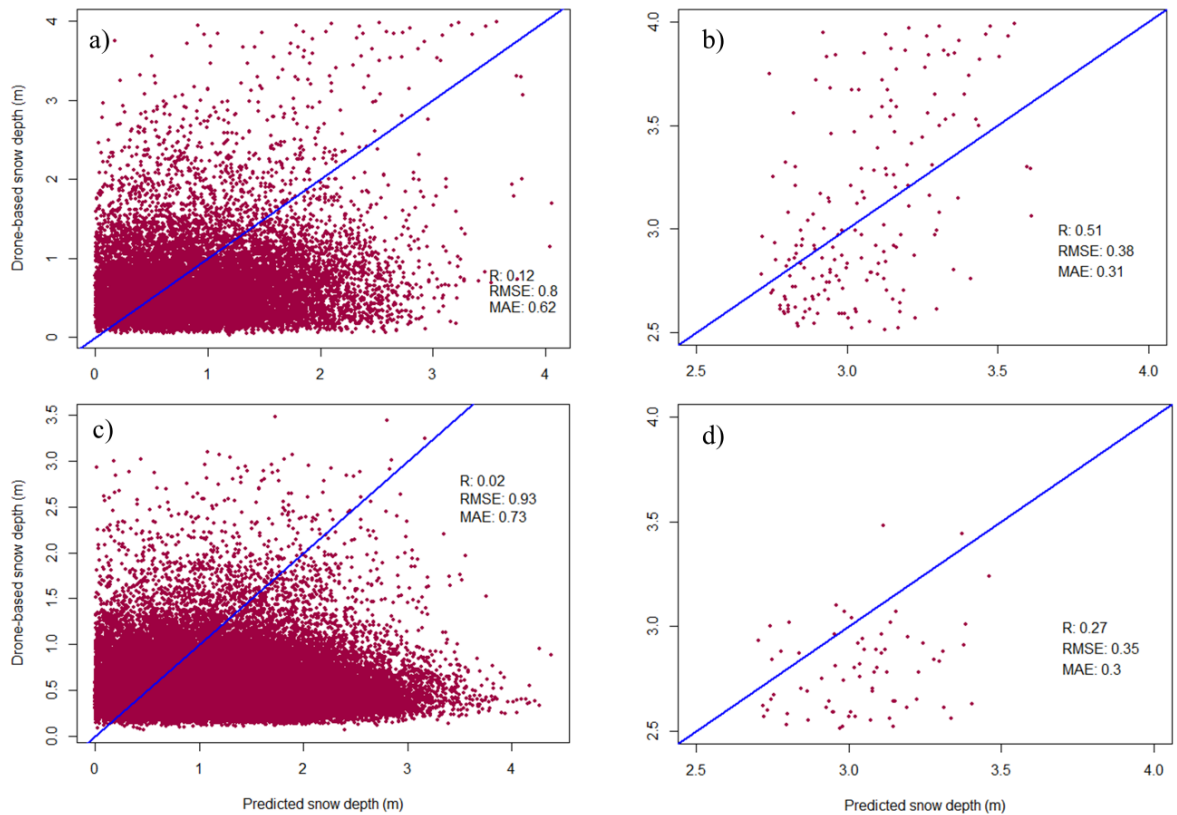

Figure 3. 12 The accuracy assessment of adjusted Lievens snow depth retrieval algorithm that validated with drone-based snow depth dataset in 2018 and 2019 under different snow depth ranges (a) the full snow depth range in 2018, (b) over 2.5 m snow depth range in 2018, (c) the full snow depth range in 2019, and (d) over 2.5 m snow depth range in 2019

53

3.5.3 Result of deep neural network

Through an extensive process of hyperparameter tuning, various model parameters—including the number of hidden layers, neurons per layer, activation function, loss function, and optimizer—were systematically optimized to identify the most effective DNN configuration. The optimal DNN architecture features one input layer, ten hidden layers, and one output layer. The input layer accommodates a number of neurons corresponding to the input variables, and in line with regression requirements, the output layer comprises a single neuron responsible for outputting the snow depth value. Each hidden layer consists of 128 neurons with a rectified linear unit (ReLU) activation function. The mean squared error (MSE) serves as the loss function, and the adaptive moment (Adam) optimizer, with a learning rate of 0.001, is employed. Given the substantial dataset size—approximately 30,000 data pairs for both training and testing—a larger batch size (1024) is employed to expedite the training process.

To evaluate the proposed DNN capacity to estimate a comprehensive range of snow depths only from C-band SAR data, there are only SAR data were used: two co-polarization backscatter (VV, HH), two cross-polarization backscatter (HV, VH), and four calculated CPRs (CPR$_{VH/VV}$, CPR$_{VH/HH}$, CPR$_{HV/VV}$, CPR$_{HVHH}$). Figure 3.13 illustrates the MSE loss trajectory during training on the training dataset, depicting the model's prediction accuracy on the testing dataset. The MSE decrease during training indicates improved prediction accuracy on the testing dataset. However, an inflection point is observed around an MSE of 0.2, suggesting challenges in learning certain features from C-band SAR data within the remaining training steps. The MSE curve plateaus at 0.09, indicating that optimal prediction accuracy is yet to be attained and underscoring the existing disparity between C-band SAR data and accurate snow depth prediction. Notwithstanding, the trained model exhibits generally inaccurate results on the testing dataset, displaying a high correlation (0.89), low RMSE (0.31 m), and MAE (0.21m). The concentration of points below 2m and around 4m is observed, with sparse representation in the 2 - 3 m range. This uneven distribution across the snow depth range may compromise the model generalization, particularly in the 2 - 3m snow depth range. Figure 3.14 presents the

snow depth estimation results for the validation dataset derived from the trained model. Comprising around 140,000 samples not utilized in the training/testing phases, the validation results exhibit a performance deterioration compared to the testing dataset, indicating potential overfitting of the model. Instances of both overestimation and underestimation are prevalent in the validation dataset, highlighting the challenges faced by the DNN in accurately estimating snow depth from the provided input variables.
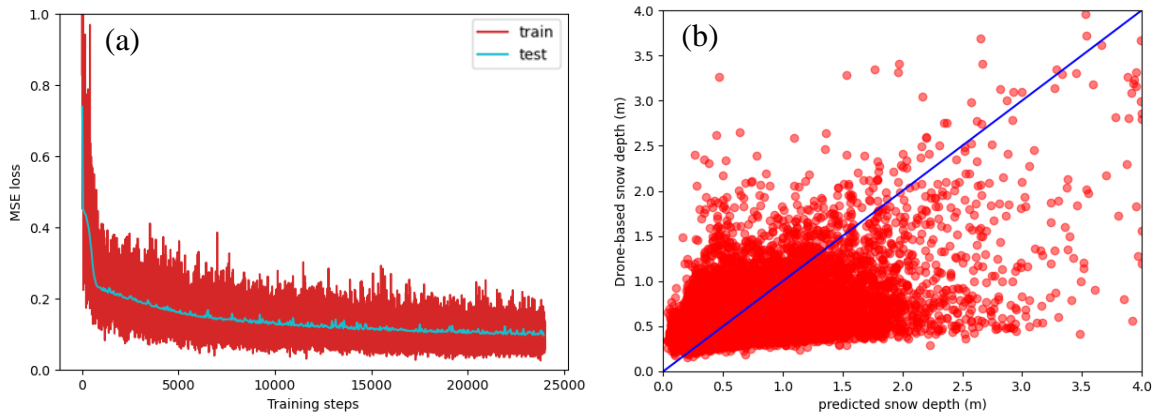
Figure 3. 13 Result of DNN model in training process with the C-band SAR data. (a) The learning curve of MSE loss change with time steps. (b) Snow depth prediction results on testing dataset.
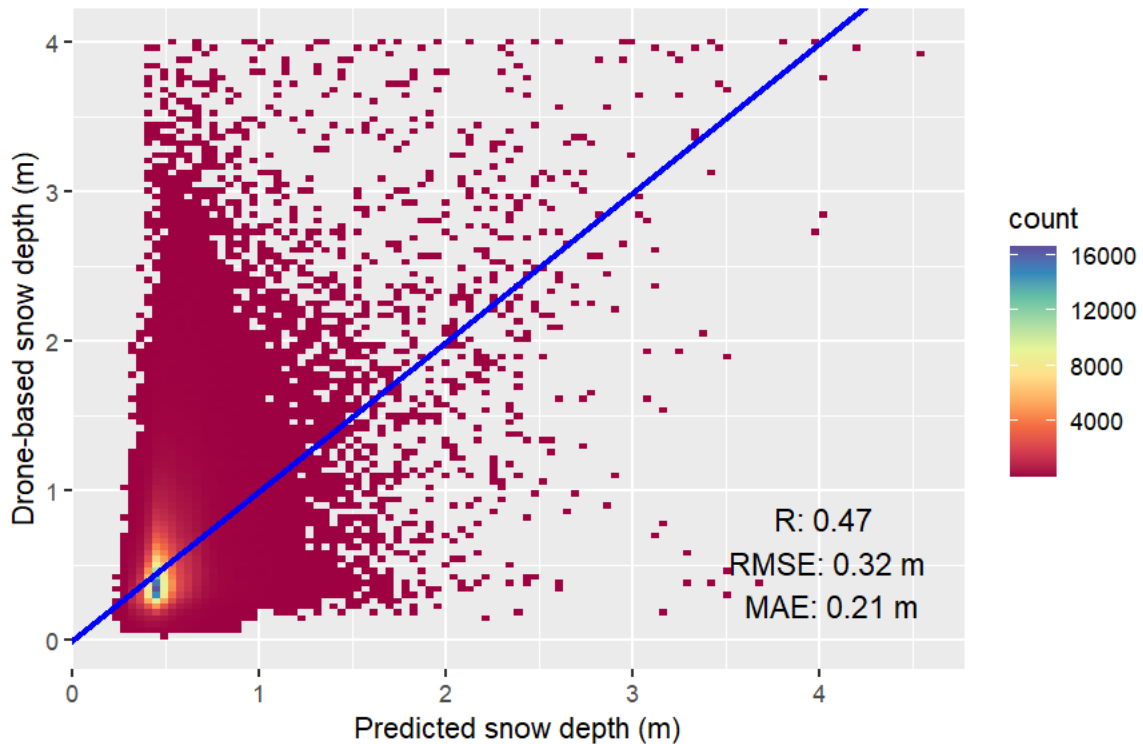
Figure 3. 14 The Result of trained DNN in validation dataset with C-band SAR data

      Given the suboptimal accuracy, higher RMSE, and MAE observed in the validation phase of the previous model, coupled with acknowledged limitations intrinsic to the DNN, it suggests challenges in elucidating relationships across the entire spectrum of snow depths using the inherently limited sensitivity of C-band SAR data. Consequently, the augmentation of input variables for the DNN model was considered. In alignment with the findings in Section 3.5.1, where it was discerned that vegetation and terrain exert influence on snow depth variations in the TVC region, five pertinent variables were incorporated: DTM, local incident angle, vegetation class, mean vegetation height, and maximum vegetation height.

      Table 3.6 provides a summary of the correlations between DTM, local incident angle, vegetation class, mean vegetation height, maximum vegetation height, and snow depth, revealing varying degrees of association with snow depth. The local incident angle, vegetation class, mean vegetation height, and maximum vegetation height were consequently integrated as additional input variables alongside C-band SAR observations in the DNN model.

Table 3. 6 The Pearson's correlation coefficient between DTM, local incident angle, vegetation class, mean vegetation height, and maximum vegetation height and snow depth in spatial dataset

	DTM	Local incident angle	Vegetation class	Mean Vegetation height	Maximum vegetation height
Snow depth	0.01	0.23	-0.33	0.30	0.27

Utilizing consistent model parameters and training procedures, the DNN was retrained by incorporating additional input variables, namely local incident angle, vegetation class, mean vegetation height, and maximum vegetation height, alongside the C-band SAR data, for the purpose of snow depth estimation. The improved DNN model underwent evaluation using the same validation dataset. Figure 3.15 provides insights into the learning curve and estimation outcomes of the revised model on the testing dataset. Notably, the MSE diminishes with increasing training steps, reaching 0.02, thereby demonstrating superior performance compared to the training process solely based on C-band SAR observations. The augmented input variables contribute to a more robust model, as evidenced by the heightened correlation (0.82) and reduced RMSE (0.17 m) and MAE (0.13 m) on the testing dataset. Figure 3.16 illustrates the estimation accuracy of the retrained DNN on the validation data, revealing a marked improvement in performance, with a notable elevation in correlation (0.79) and a concurrent reduction in RMSE (0.27 m) and MAE (0.20 m) when compared to the DNN lacking the additional terrain variables. This outcome underscores the efficacy of incorporating these pertinent variables to enhance the accuracy of snow depth estimation by the DNN model.
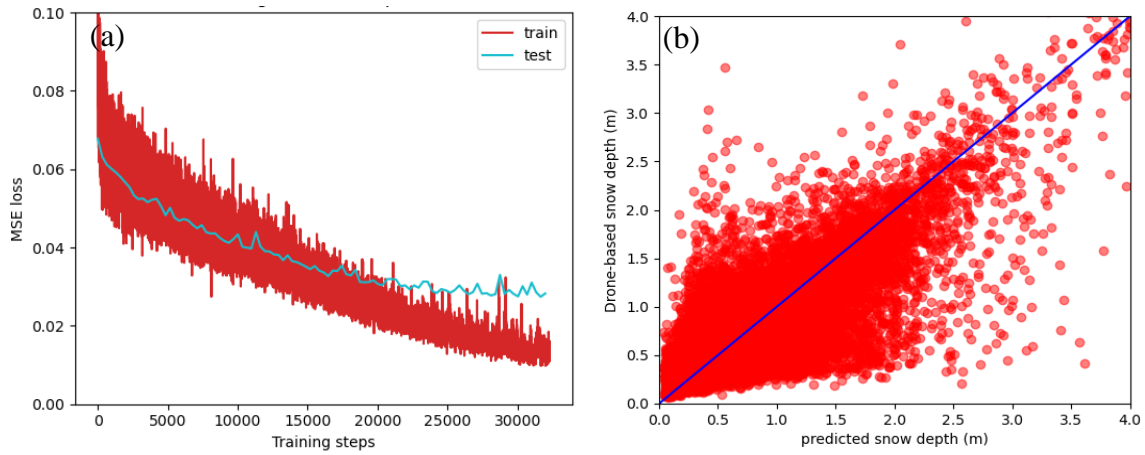
Figure 3. 15 Result of updated model in training process C-band SAR data and corresponding local incident angle, vegetation class, mean vegetation height and maximum vegetation height (a) The learning curve of MSE loss change with time steps. (b) Snow depth prediction results on testing dataset
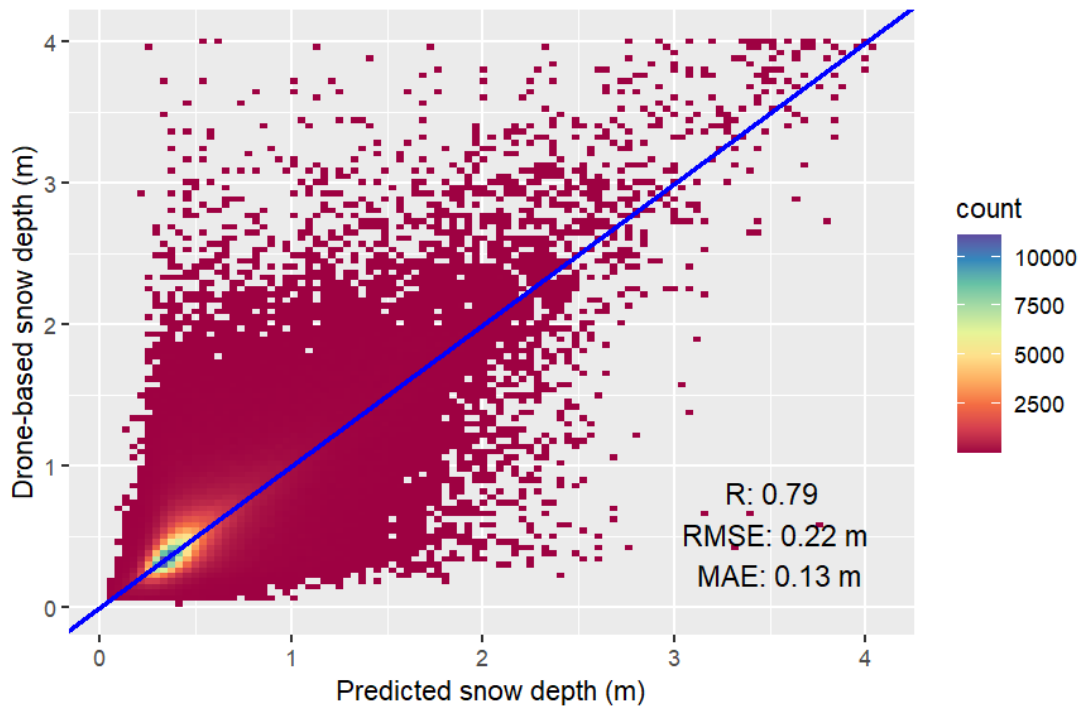
**Figure 3. 16** Result of updated model in validation dataset

To facilitate a comparative analysis between the Deep Learning and numerical approaches, the updated DNN is employed to estimate deep snow depth, utilizing the

associated input variables, at specific locations corresponding to the adjusted Lievens approach for the year 2018. Figure 3.17 showcases the estimation outcomes of the updated DNN model within deep snow depth areas in the 2018 drone-based snow depth dataset. Notably, the DNN model achieves a substantial correlation of 0.83, along with diminished RMSE at 0.29 m and MAE at 0.21 m. In stark contrast, as illustrated in Figure 3.12 (b), the adjusted Lievens approach exhibits a comparatively lower correlation of 0.51, coupled with elevated RMSE at 0.37 m and MAE at 0.3 m. This discrepancy in performance metrics emphasizes the superiority of the DL approach, leveraging C-band SAR observations, over the numerical approach in estimating both deep and shallow snow depths.
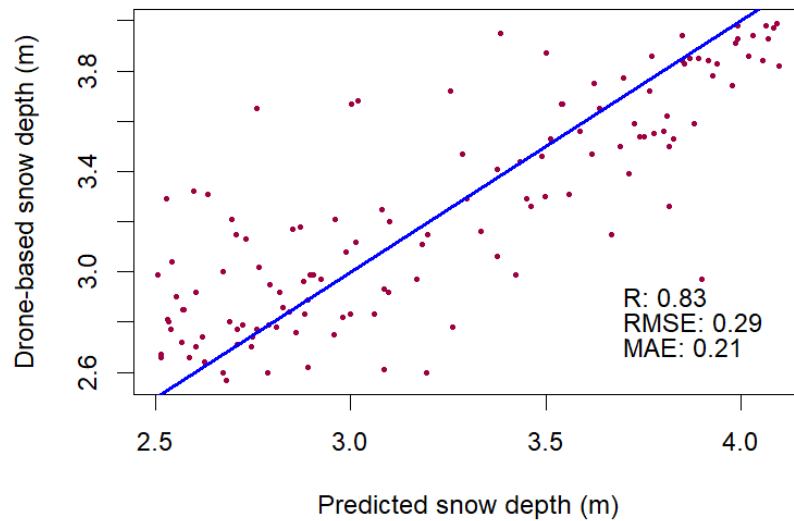
Figure 3. 17 The prediction results of the updated DNN on the same deep snow depth samples (over 2.5 meters) as the adjusted Lievens approach in 2018

Ultimately, the improved DNN model was deployed across the entire study area to prognosticate snow depth comprehensively. The outcomes are visually depicted in Figure 3.18. Notably, the anticipated deeper snow depths predominantly manifest in the gulley and drift area. It is imperative to acknowledge that, owing to the scarcity of snow depth reference data pertaining to locations with substantial snow depth, uncertainties in the predicted snow depth are inevitable. Nevertheless, the prognostication serves to offer overarching insights into the

59

identification of regions characterized by deeper snowpacks and elucidates the dynamics underlying the formation of deep snowpacks within the study area.
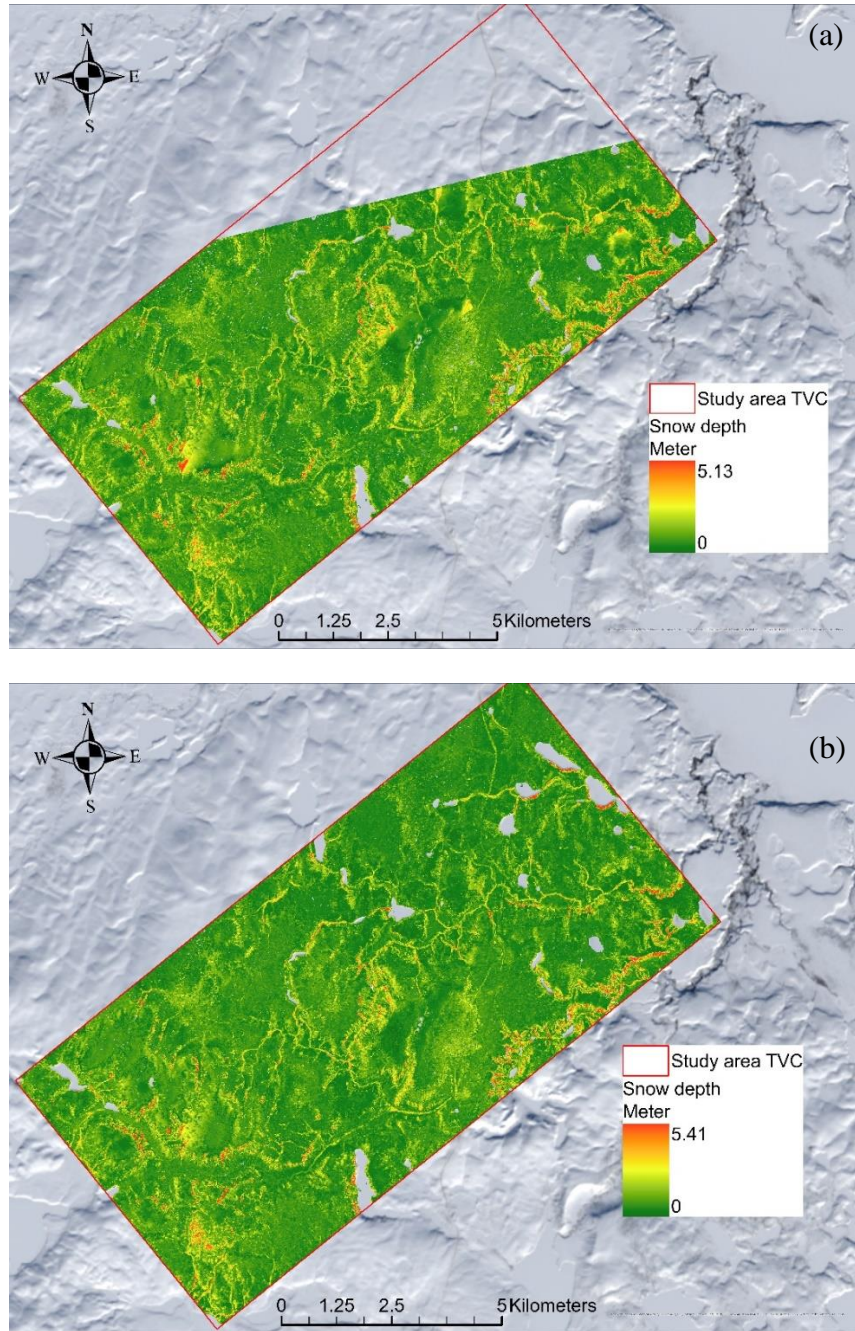
Figure 3. 18 The predicted snow depth variability map in whole study area of TVC from updated DNN model at (a) March 15, 2018, and (b) April 10, 2019

3.6 Discussion

3.6.1 The sensitivity of C-band SAR on Tundra snow

In the results of Section 3.5.1, cross-pol backscatter demonstrates sensitivity to increased snow depth, a phenomenon consistent with Lievens (2019), who suggested that cross-pol backscatter results from the interplay of volume and ground scattering, with volume scattering predominating in the presence of significant snow depths. In TVC, lower backscatter features (~ –28 dB) within the 0-1m snow depth range may arise from ground scattering outweighing volume scattering. Beyond 1m snow depth, the growing prominence of snow volume scattering renders the cross-pol backscatter more sensitive to changes in snow depth. For snow depths exceeding 2 m, the constant volume scattering resulting from heightened snow thickness becomes the dominant response from the snowpack, reinforcing the correlation between cross-pol backscatter and snow depth. Similarly, co-pol in TVC exhibits noticeable sensitivity to deep snow. In the 0-2 m snow depth range, the primary co-pol backscatter feature remains relatively constant at around -16 dB, indicating that the increase in snow thickness does not lead to a significant shift towards volume scattering dominance. This aligns with the findings of Lievens et al. (2019). In regions with snow depths exceeding 2 m, co-pol backscatter experiences a slight decreasing trend (~ 2 dB) with increasing thickness, possibly attributed to strong ground surface scattering attenuated by the deep snowpack. However, the lack of a discernible increase in co-pol backscatter suggests that ground surface scattering remains more pronounced than snow volume scattering. Consequently, the CPR derived from cross-pol and co-pol exhibits higher sensitivity to snow depth, likely due to the robust correlation between enhanced volume scattering and snow depth. The CPR, as hypothesized by Lievens et al. (2019) to mitigate the effects of ground surface, vegetation, or snow conditions, demonstrates a strong correlation with snow depth compared to individual cross-pol or co-pol backscatter. In instances where cross-pol exhibits no or limited sensitivity to snow depth, the sensitivity introduced by co-pol, especially in deep snow, contributes to the heightened sensitivity of the CPR value to snow depth.

Regarding the impact of vegetation on C-band SAR sensitivity to snow depth, assuming complete freezing of vegetation and interior water due to subzero temperatures in winter, tall vegetation such as trees, tall shrubs, riparian shrubs, and dwarf shrubs forms large irregular ice crystals, yielding high cross-pol backscatter owing to substantial volume scattering. In contrast, low vegetation types like tussocks and lichens, lacking a branch structure, fail to provide strong volume scattering, resulting in lower cross-pol backscatter. As snow accumulates on underlying vegetation, volume scattering intensifies with increasing snow thickness. The observed cross-pol backscatter variation in taller vegetation consistently exceeds -25 dB, while the variation in low vegetation areas (tussocks and lichens) remains below -25 dB, supporting these hypotheses. Co-pol backscatter, associated with frozen vegetation, tends to offer strong ground scattering, rendering it generally insensitive to shallow snow depth changes within the 0-2m range. Beyond 2m snow depth, the potential attenuation of strong ground scattering by the deeper snowpack allows for a discernible decrease in co-pol backscatter. Additionally, since snow depth distribution in TVC is closely tied to vegetation and landscape, deep snowpacks are predominant in drift and gully areas. The vegetation class map illustrates tussocks and lichens as dominant in TVC, concentrated in flat terrains where snow accumulation is challenging, resulting in shallow snow depths (less than 1m) in these regions. Conversely, tall and riparian shrubs cluster in drift and gully landscapes, facilitating the accumulation of deep snowpacks through wind-driven processes, making C-band SAR more sensitive to snow in these areas spatially and temporally.

Building on findings from other literature, C-band sensitivity to deep snow may stem from the formation of large-sized snow crystal clusters and complex snow layering structures within the deep snowpack. The irregular shape of snow crystals, highly anisotropic in nature, leads to stronger volume scattering of cross-pol, a phenomenon validated through physically based modeling (Tsang et al., 2022; Zhu et al., 2023). Since large snow crystals and complex layering are not characteristic of shallow snow depths, C-band sensitivity to such conditions is generally absent, regardless of the environment (tundra or taiga). C-band backscatter (especially co-pol) has been identified as highly sensitive to wet snow, evidenced by a

substantial decrease in backscatter (Stiles & Ulaby, 1980). However, given that the air temperature during March 2018 and April 2019, as indicated by meteorological station data (Figure 3.2), remained below 0 degrees Celsius, and measurements were taken during subfreezing periods, the study area likely did not experience the formation of wet snow. As for the observed decrease in co-pol backscatter with increasing snow depth in dry snow, this may be attributed to the strong ground surface scattering caused by the rough frozen soil/ice layer and vegetation beneath the snowpack. Some decreases in co-pol backscatter are also observed in regions where the snowpack attenuates the area with robust ground surface scattering (Shi & Dozier, 2000; Pivot, 2012). According to Lievens et al. (2022), a similar co-pol backscatter behavior concerning snow depth has been observed in the glacier area of the Alpen Mountains range. However, since these observations primarily pertain to shallow snowpacks (< 2m snow depth), deciphering the complex relationship between the decrease in co-polarization backscatter and snowpack thickness remains challenging.

3.6.2 Uncertainty in snow depth estimation from adjusted Lievens snow depth algorithms

In contrast to the Lievens approach in 2019, which utilized Sentinel-1 time series backscatter observations with a more frequent 6-day revisit interval, the employed RSAT-2 data in this study exhibits a less frequent 24-day revisit cycle. Consequently, the calculated SI derived from RSAT-2 data often yields numerous zero values at each time step, a characteristic stemming from the prolonged revisit period. The interpretation of zero SI values as indicative of snow melting or disappearance, as rationalized in the Lievens approach due to frequent occurrences in mountainous regions, faces limitations when applied to artic tundra environment. TVC experiences a low probability of snowmelt or disappearance events, given the consistently low air temperatures around 0 degrees Celsius throughout winter. Thus, the occurrence of zero SI values in TVC, owing to the ease of snow redistribution by wind, is less justifiable.

Since the SI is computed based on time series SAR data at the pixel scale, the temporal variation of the CPR may not exclusively result from changes in snow depth. In TVC, wind-driven processes emerge as the predominant mechanism driving snow depth changes, aside

from minor snowfall events. Given that most shallow snowpacks (0 – 1m) are situated in flat areas with low slopes, wind easily channels beneath the snow layer, leading to the accumulation of deeper snow. This phenomenon may contribute to the observation of minimal CPR change in shallow snow areas within the SAR time series. Conversely, mountainous regions, featuring ample locations for snow storage, exhibit more consistent temporal CPR variations.

The Lievens approach calculates the SI at a spatial resolution of 1000 m rather than the finer 10 m resolution used in drone-based snow depth data. As SAR observations typically contain radiometric errors, speckle noise inherent to radar observations, radar shadowing effects, and geometric distortions within complex topography, the coarser spatial resolution substantially mitigates these errors and effects on the actual backscatter observation of snow (Lievens et al., 2022). However, given that drone-based snow depth data indicates depths exceeding 3 m predominantly at fine spatial resolutions (1m to 10m), and the majority of snow depths fall within the 0 to 1 m range, aggregating SAR observations at 1000 m spatial resolution significantly smoothens the features associated with deep snowpacks. To retain RSAT-2 backscatter features representative of deep snowpacks, the SI must be calculated at a 10m spatial resolution. This necessitates caution as the SI, thus derived, introduces more uncertainty and errors, particularly in locations characterized by shallow snowpacks.

3.6.3 Deep learning approach Potential and Limitation with RSAT-2 data

Drawing from the sensitivity analysis, it becomes apparent that C-band backscatter observations exhibit limited sensitivity to variations in snow depth. Even CPR prove sensitive solely to depths exceeding 2 meters. This assumption lays the foundation for establishing the connection between RSAT-2 observations and snow depth. Given the demonstrated efficacy of neural networks in bridging knowledge gaps associated with C-band observations and snow depth, the cross-pol, co-pol, and CPR observations are considered sufficient for training the DNN to accurately estimate snow depth. However, the predictive capability of the trained DNN, as illustrated in Figure 3.14, falls short of accurately predicting the full range of snow depth within the validation dataset independently. The dataset still encompasses SAR observations

insensitive to snow depth, underscoring the need to include such observations as additional data features in the fully connected neural network.

Given that snow depth distribution closely correlates with terrain and vegetation cover in TVC, incorporating terrain and vegetation information (Digital Terrain Model, Local Incidence Angle, vegetation class, vegetation height) significantly enhances the prediction accuracy of the trained DNN on the validation dataset, as evidenced in Figure 3.16. As C-band SAR alone exhibits limited sensitivity to snow depth, the incorporation of additional vegetation and terrain information elucidates and substantially improves the relationship between snow depth and C-band SAR within the DNN.

In comparison to the empirical approach proposed by Lievens et al. (2019), the deep learning (DL) method excels in handling nonlinear relationships, even in scenarios where the relationship between inputs and outputs is weak. The adjusted Lievens approach, as depicted in snow depth estimation results (Figure 3.10), fails to accurately estimate snow depth across the full range due to the limited sensitivity of C-band SAR. The DL approach, however, mitigates estimation uncertainty across the entire range of snow depth, leveraging data with limited sensitivity. Moreover, DL can seamlessly integrate additional information, such as vegetation and terrain details, beyond input C-band SAR observations, yielding relatively high accuracy in estimating both shallow and deep snow.

A second advantage of the DL approach lies in its capacity to handle non-linear relationships between C-band SAR observations and snow depth without necessitating prior knowledge or a sequential time series model. Unlike Lievens et al. (2019), which required temporal CPR observations for snow index calculation and relied on an empirical index to align the snow index with actual snow depth, DL methods autonomously identify and learn relationships with sufficient snow depth data. The trained DNN can accurately predict snow depth after an adequate amount of training, eliminating the need for post-season calibration of the relationship between CPR and snow depth, both spatially and temporally.

It is crucial to note that the DL approach is inherently limited in recognizing features on which it was not trained. For instance, in a classification problem, if the model is solely

trained on classes 0 and 1, it will be unable to recognize a new class. Therefore, DNNs require numerous features and samples for effective training. However, when applied to data with similar features, the model can make accurate predictions and outperform the training dataset.

3.7 Conclusion

This research explores C-band SAR backscatter sensitivity in the Arctic tundra snow environment and aims to develop a method for deep snow depth estimation. C-band SAR is known to be sensitive to wet snow, and the CPR offers a strong correlation with snow depth, particularly in mountainous regions. To evaluate this sensitivity, the RSAT-2 SAR system is chosen for a tundra snow sensitivity analysis. RSAT-2 data exhibit sensitivity to snow depth variations between 0 and 4 meters, with cross-polarization showing a notable increase as snow depth increases, especially for depths exceeding 2 meters. The study reveals that both cross-polarization and co-polarization sensitivity become more pronounced with snow depths over 2 meters. The CPR consistently demonstrates a stronger correlation with snow depth than individual cross-polarization or co-polarization backscatter values. Furthermore, the study highlights that C-band SAR sensitivity in tundra snow aligns with findings from mountainous areas. The presence of underlying vegetation in the snowpack also affects C-band SAR sensitivity, with tall or riparian shrub areas showing heightened volume scattering in cross-polarization and strong ground scattering in co-polarization. The increased sensitivity is primarily observed in areas with tall or riparian shrubs, which tend to accumulate snow depths exceeding 3 meters, with peak snow depth typically occurring in March. With the dominant snow depth retrieval algorithm, proposed by Lievens et al. (2019), is effective in mountainous regions but requires adjustment for TVC. The adapted Lievens approach is suitable for estimating snow depths over 2.5 meters but less effective for shallower snow. Therefore, a Deep Learning (DL) approach is applied to bridge the gap between C-band SAR observations and accurate estimates of shallow and deep snow depths. As the result shown, the C-band SAR data still be limited to estimate accurate snow depth with the DNN. The DL method also can integrate with terrain and vegetation data to enhances estimation accuracy that achieved high correlation with low RMSE and MAE value. In summary, the DL method proves to be more

effective in estimating snow depth using C-band SAR observations and additional environmental data in the TVC region.

Chapter 4 Summary, Limitations, Conclusions and Future Research

4.1 Summary

This study reveals the high potential of C-band SAR, particularly RSAT-2 backscatter, for monitoring Arctic tundra snow depth at high resolution, especially deep snowpacks. This confirms our objectives of exploring SAR sensitivity and validates the suitability of both the numerical and deep learning approaches for tundra snow depth estimation. Our results support Lievens et al. (2019) observation of CPR sensitivity, further demonstrating its effectiveness in TVC with both cross-pol and co-pol contributions. However, we observed a higher threshold for sensitivity (2.5m vs. 0.5m), likely due to differences in spatial resolution and terrain. The influence of different vegetation cover on C-band sensitivity with snow depth adds another layer of complexity to the relationship. The high sensitivity is more likely exist in tall vegetation area since those areas are also overlapped with drift and gully area. Notably, throughout the time series, backscatter variation in deep snowpack locations exhibits an obvious change, suggesting the effectiveness of the CPR method in these areas.

Adapting the Lievens approach with optimized a and b coefficients yielded promising results (correlation = 0.51, MAE = 0.31 m) for locations exceeding 2.5 meters, corroborating the effectiveness of this method for deep snow accumulation areas. The large coverage of drone-based data further enabled to explore a deep learning approach using SAR data combined with geographic information like LIA, vegetation class, and height. Compared to relying solely on SAR data, this approach significantly increased the DNN estimated accuracy. Moreover, the trained DNN could generate a snow depth variability map for the entire TVC study area, providing valuable insights into spatial snow distribution and potential applications in whole arctic tundra area. However, further evaluation with additional deep snow depth measurements is necessary to refine the estimated accuracy.

This study demonstrates the potential of RSAT-2 and other C-band SAR data for monitoring dry snow depth in Arctic tundra environments, even with complex terrain. The Lievens approach, in particular, shows promise for estimating deep snow depth within drifts

68

and gullies at high resolution. However, the limited revisit frequency of RSAT-2 observations restricts the accuracy of snow depth estimates. Thus, deep learning holds promise as a better alternative, offering high accuracy even without relying on time-series data. This capability opens the door for cost-effective and widely applicable methods for Arctic-wide snow depth estimation using RSAT-2 and other spaceborne C-band SAR data.

4.2 Limitations

There are several limitations of the methodology are recognized in this study:

In the sensitivity analysis of the CPR method at TVC, the RSAT-2 data are used to generate CPR value to analyze snow depth data at the end of winter. In the research of Lievens et al. (2019), the Sentinel-1 SAR time series data are used to conduct spatial-temporal analysis between CPR and snow depth across different sites throughout the winter. Since RSAT-2 and Sentinel-1 use different SAR systems, the parameters (spatial resolution, pixel spacing, radiometric correction) of the generated SAR observation will differ, resulting in different C-band sensitivities to the same snowpack. Also, due to the lack of snow depth samples trough without the end of the winter period, the temporal correlation of CPR, cross-pol and co-pol with snow accumulation cannot be tested.

In TVC, there is a lack of spatial-temporal snow depth reference data through the winter period. Since the snow depth estimation result of the Lievens approach is validated by spatial-temporal snow depth reference through the whole winter period, the adjusted Lievens approach cannot be thoroughly evaluated at other time steps of TVC. Furthermore, as the adjusted indices a and b from Lievens approach were calculated based on the spatial-temporal in-situ observations, the a and b index are calculated by the global minima through the entire dataset. As the acquisition dates of drone-based snow depth data are concentrated in the end-of-winter period during 2018 and 2019, the a and b index from the adjusted Lieven approach is the local minima, which means the adjusted Lieven approach may not estimate accurate snow depth in other time steps.

As shown in Table 3.1, the RSAT-2 and drone-based snow depth in the spatial data set were collected on different days, which means that the actual snow depth in the SAR

observations may have a specific error with the drone-based snow depth. However, DNN requires a high precision of the reference data in the training process; these errors may cause the estimated snow depth and contain many errors with actual snow depth. Also, the DNN required a large number of samples to ensure the DNN can full captures the relation between inputs and outputs. Due to the lack of snow depth data in the TVC, there may be errors in snow depth estimates from outside the AOIs range.

4.3 Future Research Aim

Since the sensitivity of C-band SAR to dry snow has been discovered in recent years, the sensitivity of C-band to deep snow and its scattering mechanism still needs to be determined. The physically based modelling could simulate the C-band backscatter with increased snow depth (Zhu et al., 2023). So, future work will combine the physically based modelling such as DMRT (Dense Media Radiative Transfer) model to keep exploring the C-band SAR sensitivity on dry snowpack in TVC with physically explanation.

Another noteworthy constraint revolves around the precision and extent of the snow depth reference data available in the TVC region. Consequently, forthcoming research will prioritize fieldwork endeavors to acquire in situ snow depth datasets. Furthermore, these field activities can yield a wealth of additional snow-related parameters, including snow density, grain size, and snow layering, which will serve as valuable references for the analysis of spatial-temporal backscatter patterns. With an augmented pool of snow depth reference data, future investigations will involve continued assessment of the Lievens et al. (2019) approach across various winter periods or the development of a new technique that leverages the Lievens approach for a more precise estimation of snow depth in TVC.

Today, X-band SAR has been available on a global scale, and the X-band cross-pol ratio may be more sensitive to snowpack properties like SWE and snow density than the C-band, especially for shallower snow (Shi & Dozier, 2000). With more snow depth reference data, future work will keep testing the Lievens approach in TVC with other times of winter period or develop a new method to accurately estimate snow death in TVC with X-band based on the Lievens approach.

As the DNN result shows, the DL method has a high potential to estimate the snow depth from C-band SAR despite the weak relation and high uncertainty between C-band SAR observation and snow depth. Today, many new structures of DNN have been developed, such as convolutional neural networks (CNNs), autoencoders (AE), recurrent neural networks (RNNs), and generative adversarial networks (GANs). The future work aims to apply different DNNs to estimate snow depth in TVC from SAR data.

4.4 Conclusions

This research aims to explore the current spaceborne C-band SAR backscatter sensitivity in the Arctic tundra snow environment and define a suitable approach for estimating deep snow depth through the tundra environment. As shown in earlier studies, dry snow is transparent to C-band SAR observations and C-band values are sensitive to wet snow. With the development of the C-band SAR system, the C-band SAR observation from the new system showed a significant sensitivity to snow depth within the mountainous range. Also, the ratio of cross-pol and co-pol (CPR) method could partially eliminate the effects of ground condition, underlying vegetation, and snow properties in the observed snowpack, which leads to a strong correlation of CPR to snow depth.

Based on these assumptions of C-band SAR to snow depth, the RSAT-2 SAR system is chosen to perform a sensitivity analysis on a tundra snow environment. In general, RSAT-2 data could show sensitivity to snow depth variation between 0 to 4 m, either cross-pol or co-pol backscatter observation. More specifically, the cross-pol backscatter generally has a noticeable increase with snow depth increase, but the co-pol backscatter shows a slightly decreasing trend with the over 2 m snow depth. It is noteworthy that cross-pol and co-pol sensitivity become more potent when the observed snow depth is over 2m. Taking the CPR also provides a stronger correlation with snow depth, which is always greater than a single cross-pol or co-pol backscatter. Therefore, C-band SAR sensitivity in tundra snow is consistent with some results in mountainous areas. The underlying vegetation in snowpack also has specific effects on C-band SAR sensitivity. The snowpack in tall or riparian shrub areas likely causes more robust volume scattering in cross-pol and strong ground scattering in co-pol,

71

making the high sensitivity only observed in tall or riparian shrubs. The tall or riparian shrubs are clustered in drift and gulley areas, which may have more opportunity to accumulate over 3 m snowpack. The temporal variation of RSAT-2 observation also proved that snow accumulation events can only be observed in the over 3 m snow depth, and the peak snow depth may only exist in March.

Currently, the most dominant snow depth retrieval algorithm from C-band SAR observation has been proposed by Lievens et al. (2019); the relatively high retrieval accuracy of snow depth can only be obtained within mountain ranges and for deeper snow, and the algorithm performance in other places still needs to be assessed. So, the numerical approach from Lievens et al. (2019) has been investigated and adjusted with suitable parameters in the TVC. The adjusted Lievens approach should be valid for estimating over 2.5 m snow depth and may not work within shallow snow. At the end of winter, the deep snow depth retrieval accuracy in March 2018 was better than in April 2019, which may cause by the different C-band SAR sensitivity to snow depth change.

Since the adjusted Lievens algorithm has a larger uncertainty when applied to estimate shallow snow, the DL approach was applied to fill the gap between C-band SAR observation and accurate shallow or deep snow depth. Concerning the DL approach, the DL method cannot accurately estimate the full range of snow depth from the C-band SAR backscatter observations. However, the snow depth distribution was found to be highly related to the terrain and vegetation in TVC; the terrain and underlying vegetation information are the additional inputs of SAR observation to trained DNN. The result of trained DNN shows that the terrain and vegetation information can enhance the estimation accuracy. In conclusion, the DL method is more suitable for estimating snow depth with C-band SAR observation and additional information at TVC.

References

Anantrasirichai, N., Biggs, J., Albino, F., Hill, P., & Bull, D. (2018). Application of machine learning to classification of volcanic deformation in routinely generated InSAR data. *Journal of Geophysical Research: Solid Earth*, *123*(8), 6592-6606.

Anders, K., Antonova, S., Boike, J., Gehrmann, M., Hartmann, J., Helm, V., ... & Sachs, T. (2018). Airborne laser scanning (ALS) point clouds of Trail Valley Creek, NWT, Canada (2016). *PANGAEA*.

Armstrong, R. L., & Brun, E. (Eds.). (2008). Snow and climate: physical processes, surface energy exchange and modeling. *Cambridge University Press*.

Awasthi, S., & Varade, D. (2021). Recent advances in the remote sensing of alpine snow: A review. *GIScience & Remote Sensing*, *58*(6), 852-888.

Barnett, T. P., Adam, J. C., & Lettenmaier, D. P. (2005). Potential impacts of a warming climate on water availability in snow-dominated regions. *Nature*, *438*(7066), 303-309.

Bernier, M., Fortin, J. P., Gauthier, Y., Gauthier, R., Roy, R., & Vincent, P. (1999). Determination of snow water equivalent using RADARSAT SAR data in eastern Canada.*Hydrological Processes*,*13*(18), 3041-3051.

Bormann, K. J., Brown, R. D., Derksen, C., & Painter, T. H. (2018). Estimating snow-cover trends from space. *Nature Climate Change*, *8*(11), 924-928.

Boike, J., & Grünberg, I. (2019). Vegetation map of Trail Valley Creek, Northwest Territories, Canada.

Chang, A. T. C., Foster, J. L., Hall, D. K., Rango, A., & Hartline, B. K. (1982). Snow water equivalent estimation by microwave radiometry. *Cold Regions Science and Technology*, *5*(3), 259-267.

Chen, S., & Wang, H. (2014, October). SAR target recognition based on deep learning. In *2014 International Conference on Data Science and Advanced Analytics (DSAA)* (pp. 541-547). IEEE.

Dai, X., Huo, Z., & Wang, H. (2011). Simulation for response of crop yield to soil moisture and salinity with artificial neural network. *Field Crops Research*,*121*(3), 441-449.

DeBeer, C. M., & Pomeroy, J. W. (2017). Influence of snowpack and melt energy heterogeneity on snow cover depletion and snowmelt runoff simulation in a cold mountain environment. *Journal of hydrology*, *553*, 199-213.

Derksen, C., Silis, A., Sturm, M., Holmgren, J., Liston, G. E., Huntington, H., & Solie, D. (2009). Northwest Territories and Nunavut snow characteristics from a subarctic traverse: Implications for passive microwave remote sensing. *Journal of Hydrometeorology*, *10*(2), 448-463.

Derksen, C., & Brown, R. (2012). Spring snow cover extent reductions in the 2008–2012 period exceeding climate model projections. *Geophysical Research Letters*, 39(19).

Dutch, V. R., Rutter, N., Wake, L., Sandells, M., Derksen, C., Walker, B., ... & Boike, J. (2022). Impact of measured and simulated tundra snowpack properties on heat transfer. *The Cryosphere*, *16*(10), 4201-4222.

Environment Canada. (2016). Canadian Climate Normals. Retrieved June 01, 2016, from http://climate.weather.gc.ca/climate_normals/index_e.html.

ESA. (2023). Sentinel-1 SAR Technical Guide. Retrieved from https://sentinels.copernicus.eu/web/sentinel/technical-guides/sentinel-1-sar

Foster, J. L., Hall, D. K., Eylander, J. B., Riggs, G. A., Nghiem, S. V., Tedesco, M., ... & Choudhury, B. (2011). A blended global snow product using visible, passive microwave and scatterometer satellite data. *International journal of remote sensing*, *32*(5), 1371-1395.

Fontrodona Bach, A., Van der Schrier, G., Melsen, L. A., Klein Tank, A. M. G., & Teuling, A. J. (2018). Widespread and accelerated decrease of observed mean and extreme snow depth over Europe. *Geophysical Research Letters*, *45*(22), 12-312.

Groisman, P. Y., Karl, T. R., Knight, R. W., & Stenchikov, G. L. (1994). Changes of snow cover, temperature, and radiative heat balance over the Northern Hemisphere. *Journal of Climate*, *7*(11), 1633-1656.

Hallikainen M. 1977. Dielectric properties of sea ice at microwave frequencies. *NASA STI/Recon Technical Report N*. 781:11293.

Hughes, L. H., Schmitt, M., Mou, L., Wang, Y., & Zhu, X. X. (2018). Identifying corresponding patches in SAR and optical images with a pseudo-siamese CNN. *IEEE Geoscience and Remote Sensing Letters*, *15*(5), 784-788.

IPCC, (2023): *Climate Change 2023: Synthesis Report.* Contribution of Working Groups I, II and III to the Sixth Assessment Report of the Intergovernmental Panel on Climate Change [Core Writing Team, H. Lee and J. Romero (eds.)]. IPCC, Geneva, Switzerland, pp. 35-115, doi: 10.59327/IPCC/AR6-9789291691647

Kinar, N. J., & Pomeroy, J. W. (2015). Measurement of the physical properties of the snowpack. *Reviews of Geophysics*, *53*(2), 481-544.

King, J., Kelly,R., Kasurak, A., Duguay, C., Gunn, G., Rutter, N., ... & Derksen, C. (2015). Spatio-temporal influence of tundra snow properties on Ku-band (17.2 GHz) backscatter. *Journal of Glaciology*,*61*(226), 267-279.

Kunkel, K. E., Robinson, D. A., Champion, S., Yin, X., Estilow, T., & Frankson, R. M. (2016). Trends and extremes in Northern Hemisphere snow characteristics. *Current Climate Change Reports*, *2*, 65-73

Li, Y., Chen, Y., Wang, F., He, Y., & Li, Z. (2020). Evaluation and projection of snowfall changes in High Mountain Asia based on NASA's NEX-GDDP high-resolution daily downscaled dataset. *Environmental Research Letters*, 15(10), 104040.

Lievens, H., Demuzere, M., Marshall, H. P., Reichle, R. H., Brucker, L., Brangers, I., ... & De Lannoy, G. J. (2019). Snow depth variability in the Northern Hemisphere mountains observed from space. *Nature communications*, *10*(1), 4629.

Lievens, H., Brangers, I., Marshall, H. P., Jonas, T., Olefs, M., & De Lannoy, G. (2022). Sentinel-1 snow depth retrieval at sub-kilometer resolution over the European Alps. *The Cryosphere*, *16*(1), 159-177.

Liu, Y., Fang, Y., & Margulis, S. A. (2021). Spatiotemporal distribution of seasonal snow water equivalent in High-Mountain Asia from an 18-year Landsat-MODIS era snow reanalysis dataset. *The Cryosphere Discussions*, *2021*, 1-25.

Luojus, K., Pulliainen, J., Takala, M., Lemmetyinen, J., Mortimer, C., Derksen, C., ... & Venäläinen, P. (2021). GlobSnow v3. 0 Northern Hemisphere snow water equivalent dataset. *Scientific Data*, *8*(1), 163

Ma, L., Liu, Y., Zhang, X., Ye, Y., Yin, G., & Johnson, B. A. (2019). Deep learning in remote sensing applications: A meta-analysis and review.*ISPRS journal of photogrammetry and remote sensing*,*152*, 166-177.

Macelloni, G., Brogioni, M., Montomoli, F., & Fontanelli, G. (2012). Effect of forests on the retrieval of snow parameters from backscatter measurements. *European Journal of Remote Sensing*, *45*(1), 121-132.

Mätzler, C., & Schanda, E. (1984). Snow mapping with active microwave sensors. *Remote Sensing*, 5(2), 409-422.

MDA (2018). RADARSAT-2 PRODUCT DESCRIPTION. Retrieved from https://earth.esa.int/eogateway/documents/20142/0/Radarsat-2-Product-description.pdf/f2783c7b-6a22-cbe4-f4c1-6992f9926dca

Mote, P. W., Li, S., Lettenmaier, D. P., Xiao, M., & Engel, R. (2018). Dramatic declines in snowpack in the western US. *Npj Climate and Atmospheric Science*, *1*(1), 2.

Mudryk, L. R., Kushner, P. J., Derksen, C., & Thackeray, C. (2017). Snow cover response to temperature in observational and climate model ensembles. *Geophysical Research Letters*, 44(2), 919-926.

Mudryk, L. R., Derksen, C., Howell, S., Laliberté, F., Thackeray, C., Sospedra-Alfonso, R., ... & Brown, R. (2018). Canadian snow and sea ice: historical trends and projections. *The Cryosphere*, *12*(4), 1157-1176.

Müller, A. C., & Guido, S. (2016). *Introduction to machine learning with Python: a guide for data scientists*. " O'Reilly Media, Inc.".

Nagler, T., & Rott, H. (2000). Retrieval of wet snow by means of multitemporal SAR data. *IEEE Transactions on Geoscience and Remote Sensing*, *38*(2), 754-765.

Nagler, T., Rott, H., Ripper, E., Bippus, G., & Hetzenecker, M. (2016). Advancements for Snowmelt Monitoring by Means of Sentinel-1 SAR. *Remote Sensing*, *8*(4), 348.

Natural Resources of Canada. (2015). *Radar Polarimetry*. Retrieved from http://www.nrcan.gc.ca/node/9275

Odry, J., Boucher, M. A., Cantet, P., Lachance-Cloutier, S., Turcotte, R., & St-Louis, P. Y. (2020). Using artificial neural networks to estimate snow water equivalent from snow depth. *Canadian Water Resources Journal/Revue canadienne des ressources hydriques*, *45*(3), 252-268.

Parikh, H., Patel, S., & Patel, V. (2020). Classification of SAR and PolSAR images using deep learning: A review. *International Journal of Image and Data Fusion*, *11*(1), 1-32

Paloscia, S., Pampaloni, P., Pettinato, S., & Santi, E. (2008). A comparison of algorithms for retrieving soil moisture from ENVISAT/ASAR images.*IEEE Transactions on Geoscience and Remote Sensing*,*46*(10), 3274-3284.

Pettinato, S., Santi, E., Brogioni, M., Paloscia, S., Palchetti, E., & Xiong, C. (2012). The potential of COSMO-SkyMed SAR images in monitoring snow cover characteristics. *IEEE Geoscience and Remote Sensing Letters*,*10*(1), 9-13.

Pomeroy, J. W., Marsh, P., & Gray, D. M. (1997). Application of a distributed blowing snow model to the Arctic. *Hydrological processes*, *11*(11), 1451-1464.

Pomeroy, J. W., Bewley, D. S., Essery, R. L., Hedstrom, N. R., Link, T., Granger, R. J., ... & Janowicz, J. R. (2006). Shrub tundra snowmelt. *Hydrological Processes: An International Journal*, *20*(4), 923-941.

Pohl, S., & Marsh, P. (2006). Modelling the spatial–temporal variability of spring snowmelt in an arctic catchment. *Hydrological Processes: An International Journal*, *20*(8), 1773-1792.

Pivot, F. C. (2012). C-band SAR imagery for snow-cover monitoring at Treeline, Churchill, Manitoba, Canada. *Remote Sensing*, *4*(7), 2133-2155

Quinton, W. L., & Marsh, P. (1998). The influence of mineral earth hummocks on subsurface drainage in the continuous permafrost zone. *Permafrost and Periglacial Processes*, *9*(3), 213-228.

Rizzoli, P., & Bräutigam, B. (2014). Radar backscatter modeling based on global tandem-x mission data. *IEEE Transactions on Geoscience and Remote Sensing*, *52*(9), 5974-5988.

Rosenfeld, D. (2000). Suppression of rain and snow by urban and industrial air pollution. *Science*, *287*(5459), 1793-1796.

Rott H, Mätzler C, Strobl D, BruzziS, Lenhart KB. (1988). Study on SAR land applications for snow and glacier monitoring. *ESA Contract Report* 6618 185 IFIFL (SC)

Rott, H., & Nagler, T. (1994). Capabilities of ERS-1 SAR for snow and glacier monitoring in alpine areas. *European Space Agency Publications ESA Sp*, *361*, 965-965.

Rott, H., Yueh, S. H., Cline, D. W., Duguay, C., Essery, R., Haas, C., ... & Nagler, T. (2010). Cold regions hydrology high-resolution observatory for snow and cold land processes. *Proceedings of the IEEE*, *98*(5), 752-765.

Sano, E. E., Matricardi, E. A. T., & Camargo, F. F. (2020). Estado da Arte do Sensoriamento Remoto de Radar: Fundamentos, Sensores, Processamento de Imagens e Aplicações. *Revista Brasileira de Cartografia*, *72*, 1458-1483.

Santi, E., Brogioni, M., Leduc-Leballeur, M., Macelloni, G., Montomoli, F., Pampaloni, P., ... & Kern, M. (2021). Exploiting the ANN potential in estimating snow depth and snow water equivalent from the airborne SnowSAR data at X-and Ku-bands. *IEEE Transactions on Geoscience and Remote Sensing*, *60*, 1-16.

Shi, J., & Dozier, J. (1997). Mapping seasonal snow with SIR-C/X-SAR in mountainous areas. *Remote Sensing of Environment*, 59(2), 294-307.

Shi, J., & Dozier, J. (2000). Estimation of snow water equivalence using SIR-C/X-SAR, part II: Inferring snow depth and particle size. *IEEE Transactions on Geoscience and Remote sensing, 38*(6), 2475-2488.

Small, D. (2011). Flattening gamma: Radiometric terrain correction for SAR imagery. *IEEE Transactions on Geoscience and Remote Sensing*, *49*(8), 3081-3093.

Smith, T., & Bookhagen, B. (2018). Changes in seasonal snow water equivalent distribution in High Mountain Asia (1987 to 2009). *Science advances*, *4*(1), e1701550.

Sturm, M., & Benson, C. (2004). Scales of spatial heterogeneity for perennial and seasonal snow layers. *Annals of Glaciology*, *38*, 253-260.

Sturm, M., Taras, B., Liston, G. E., Derksen, C., Jonas, T., & Lea, J. (2010). Estimating snow water equivalent using snow depth data and climate classes. *Journal of Hydrometeorology*, *11*(6), 1380-1394.

Sturm, M., Goldstein, M. A., & Parr, C. (2017). Water and life from snow: A trillion dollar science question. *Water Resources Research*, 53(5), 3534-3544.

Touzi, R., Vachon, P. W., & Wolfe, J. (2010). Requirement on antenna cross-polarization isolation for the operational use of C-band SAR constellations in maritime surveillance. *IEEE Geoscience and Remote Sensing Letters*, *7*(4), 861-865.

Tsang, L., Durand, M., Derksen, C., Barros, A. P., Kang, D. H., Lievens, H., ... & Xu, X. (2021). Global Monitoring of Snow Water Equivalent using High Frequency Radar Remote Sensing. *The Cryosphere Discussions,* 2021, 1-57.

Tsai, Y. L. S., Dietz, A., Oppelt, N., & Kuenzer, C. (2019). Remote sensing of snow cover using spaceborne SAR: A review. *Remote Sensing*, *11*(12), 1456.

Trail Valley Creek Arctic Research Station. (2023). Retrieved from https://www.trailvalleycreek.ca/

Ulaby, F. T., & Stiles, W. H. (1981). Microwave response of snow. *Advances in Space Research*, 1(10), 131-149.

Ulaby, F. T., Stiles, W. H., & AbdelRazik, M. (1984). Snowcover influence on backscattering from terrain. *IEEE Transactions on geoscience and remote sensing*, (2), 126-133.

Vekom. (2023). Retrieved from https://vekom.com/wp-content/uploads/2020/12/Capella_Space_SAR_Imagery_Products_Guide.pdf

Wang, P., Zhang, H., & Patel, V. M. (2017). SAR image despeckling using a convolutional neural network. *IEEE Signal Processing Letters*, *24*(12), 1763-1767.

Wang, W. (2022). Snow Depth Retrieval from Wide Band Radar in Trail Valley Creek (Master's thesis, University of Waterloo).

Walker, B., Wilcox, E. J., & Marsh, P. (2020). Accuracy assessment of late winter snow depth mapping for tundra environments using Structure-from-Motion photogrammetry. *Arctic Science*, *7*(3), 588-604.

Woodhouse, I. H. (2006). *Introduction to Microwave Remote Sensing.* CRC, New York.

Yueh, S. H., Dinardo, S. J., Akgiray, A., West, R., Cline, D. W., & Elder, K. (2009). Airborne Ku-band polarimetric radar remote sensing of terrestrial snow cover. *IEEE Transactions on Geoscience and Remote Sensing*,*47*(10), 3347-3364.

Zhang, L., Zhang, L., & Du, B. (2016). Deep learning for remote sensing data: A technical tutorial on the state of the art. *IEEE Geoscience and remote sensing magazine*, *4*(2), 22-40.

Zhu, X. X., Tuia, D., Mou, L., Xia, G. S., Zhang, L., Xu, F., & Fraundorfer, F. (2017). Deep learning in remote sensing: A comprehensive review and list of resources. *IEEE geoscience and remote sensing magazine*, *5*(4), 8-36.

Zhu, X. X., Montazeri, S., Ali, M., Hua, Y., Wang, Y., Mou, L., ... & Bamler, R. (2021). Deep learning meets SAR: Concepts, models, pitfalls, and perspectives. *IEEE Geoscience and Remote Sensing Magazine*, *9*(4), 143-172.

Zhu, J., Tsang, L., & Liao, T. H. (2021, December). Scattering from Random Rough Surfaces at X and Ku band for Global Remote Sensing of Terrestrial Snow. In *2021 IEEE International Symposium on Antennas and Propagation and USNC-URSI Radio Science Meeting (APS/URSI)* (pp. 1115-1116). IEEE.

Zhu, J., Tsang, L., & Xu, X. (2023). Modeling of Scattering by Dense Random Media Consisting of Particle Clusters With DMRT Bicontinuous. *IEEE Transactions on Antennas and Propagation.*